

The properties of cooling flows in X-ray luminous clusters of galaxies

S.W. Allen

Institute of Astronomy, Madingley Road, Cambridge CB3 OHA

October 30, 2018

ABSTRACT

We discuss the X-ray properties of the cooling flows in a sample of thirty highly X-ray luminous clusters of galaxies observed with the ASCA and ROSAT satellites. We demonstrate the need for multiphase models to consistently explain the spectral and imaging X-ray data for the clusters. The mass deposition rates of the cooling flows, independently determined from the ASCA spectra and ROSAT images, exhibit good agreement and exceed $1000 M_{\odot} \text{ yr}^{-1}$ in the largest systems. We confirm the presence of intrinsic X-ray absorption in the clusters using a variety of spectral models. The measured equivalent hydrogen column densities of absorbing material are sensitive to the spectral models used in the analysis, varying from average values of a few $10^{20} \text{ atom cm}^{-2}$ for a simple isothermal emission model, to a few $10^{21} \text{ atom cm}^{-2}$ using our preferred cooling flow models, assuming in each case that the absorber lies in a uniform foreground screen. The true intrinsic column densities are likely to be even higher if the absorbing medium is distributed throughout the clusters. We summarize the constraints on the nature of the X-ray absorber from observations in other wavebands. A significant part of the X-ray absorption may be due to dust.

Key words: galaxies: clusters: general – cooling flows – intergalactic medium – X-rays: galaxies

1 INTRODUCTION

X-ray observations of clusters of galaxies show that in the central regions of most clusters the cooling time of the intracluster gas is significantly less than a Hubble time (e.g. Edge, Stewart & Fabian 1992; White, Jones & Forman 1997; Peres *et al.* 1998). This cooling is thought to lead to a slow net inflow of material towards the cluster centre; a process known as a cooling flow (see Fabian 1994 for a review). X-ray imaging data show that gas typically ‘cools out’ throughout the central few tens to hundreds of kpc in clusters, with $\dot{M}(r) \propto r$, where $\dot{M}(r)$ is the integrated mass deposition rate within radius r (e.g. Thomas, Fabian & Nulsen 1987). Spatially resolved X-ray spectroscopy has confirmed the presence of distributed cooling gas in cooling flows, with a spatial distribution and luminosity in good agreement with the predictions from the imaging data and cooling-flow models (e.g. Allen & Fabian 1997).

For some years, the primary uncertainty with the standard model for cooling flows was the fate of the cooled matter (e.g. see Fabian, Nulsen & Canizares 1991). However, the discovery of large column densities of intrinsic X-ray absorbing material associated with cooling flows observed with the Solid State Spectrometer (SSS) on the Einstein Observatory (White *et al.* 1991; Johnstone *et al.* 1992) opened one inter-

esting possibility. Follow-up spatially-resolved X-ray spectroscopy with the Position Sensitive Proportional Counter (PSPC) on ROSAT (e.g. Allen *et al.* 1993; Irwin & Sarazin 1995; Allen & Fabian 1997) confirmed the presence of intrinsic X-ray absorbing material in cooling-flow clusters and further showed this material to be distributed throughout, but centrally-concentrated within, the cooling flows. The X-ray data thus identify the intrinsic X-ray absorbing material as a plausible sink for the cooled gas deposited by the cooling flows.

In this paper we examine the X-ray properties of the cooling flows in a sample of 30 of the most X-ray luminous ($L_{\text{Bol}} > 10^{45} \text{ erg s}^{-1}$) clusters of galaxies known. Using ASCA spectra and ROSAT High Resolution Imager (HRI) data, we present independent determinations of the mass deposition rates in the cooling flows and measure the column densities of intrinsic X-ray absorbing material associated with these systems. We show that the cooling flow model provides a consistent description of the X-ray imaging and spectral data and that the observed masses of intrinsic X-ray absorbing material are in reasonable agreement with the masses expected to have been accumulated by the cooling flows over their lifetimes. We also discuss the evidence for mass deposition from the cooling flows in other wavebands.

This is the final paper in a series that has examined

the impact of cooling flows on mass measurements (Allen 1998), the $kT_X - L_{\text{bol}}$ relation (Allen & Fabian 1998a) and metallicity measurements (Allen & Fabian 1998b) for X-ray luminous clusters. In this paper, we describe the data reduction and analysis procedures used in these works. A large number of other, previous studies have also analysed one or more of data sets included here (see references in the papers listed above), although these studies have not, in general, examined the properties of the cooling flows in the clusters. Exceptions are the deprojection analysis of Peres *et al.* (1998), and the combined ASCA/ROSAT studies of Allen *et al.* (1996), Schindler *et al.* (1997), Böhringer *et al.* (1998) and Rizza *et al.* (1998).

The cosmological parameters $H_0 = 50 \text{ km s}^{-1} \text{ Mpc}^{-1}$, $\Omega = 1$ and $\Lambda = 0$ are assumed throughout.

2 OBSERVATIONS AND DATA REDUCTION

2.1 Sample selection

Our sample was identified from clusters contained in the ROSAT X-ray Brightest Abell-type Cluster Sample (XBACS; Ebeling *et al.* 1996) and ROSAT Brightest Cluster Sample (BCS; Ebeling *et al.* 1998) with X-ray luminosities in the $0.1 - 2.4 \text{ keV}$ band exceeding $10^{15} \text{ erg s}^{-1}$. From this initial list, we selected for study those targets with ASCA X-ray spectra and ROSAT High Resolution Imager (HRI) data available on the Goddard Space Flight Centre (GSFC) public archive as of 1997 July 15. We supplemented this sample with a number of other, southern X-ray luminous clusters, known to exhibit strong gravitational lensing effects (PKS0745-191, RXJ1347.5-1145, MS2137.3-2353, AC114) and the distant, luminous cooling-flow clusters Abell 1068, 1704 and IRAS 09104+4109.

The primary goal of this project was to investigate the X-ray properties of cooling flows in X-ray luminous clusters and their effects on the integrated X-ray properties of their host systems. We have not included either the Perseus (Abell 426) or Coma (Abell 1656) clusters in our study, although these systems met our selection criteria, since both are too close ($z = 0.0183$ and 0.0232 , respectively) to allow their integrated cluster properties to be studied using the techniques used in this paper. Detailed analyses of these clusters and other nearby cooling flows are discussed by Allen *et al.* (1999).

The clusters Abell 370, 115 and 1758 also met the selection criteria but were not included in our study since ROSAT HRI images show them not to be single, coherent structures but to consist of a number of merging subunits. The integrated X-ray spectra for such clusters will relate to the virial properties of the individual subclusters rather than the systems as a whole, and the assumptions of spherical symmetry and hydrostatic equilibrium required by the X-ray modeling will not apply. The X-ray images for the other clusters included in the sample do not exhibit any dramatic substructure that would suggest these assumptions to be invalid. Our final sample consists of 30 clusters, spanning the redshift range $0.056 < z < 0.451$, with a mean redshift of 0.21.

2.2 The ASCA observations

The ASCA (Tanaka, Inoue & Holt 1994) observations were made over a three-and-a-half year period between 1993 April and 1996 December. The ASCA X-ray Telescope array (XRT) consists of four nested-foil telescopes, each focussed onto one of four detectors; two X-ray CCD cameras, the Solid-state Imaging Spectrometers (SIS; S0 and S1), and two Gas scintillation Imaging Spectrometers (GIS; G2 and G3). The XRT provides a spatial resolution of $\sim 3 \text{ arcmin}$ Half Power Diameter (HPD) in the energy range $0.3 - 12 \text{ keV}$. The SIS detectors provide good spectral resolution [$\Delta E/E = 0.02(E/5.9\text{keV})^{-0.5}$] over a $22 \times 22 \text{ arcmin}^2$ field of view. The GIS detectors provide poorer energy resolution [$\Delta E/E = 0.08(E/5.9\text{keV})^{-0.5}$] but cover a larger circular field of view of $\sim 50 \text{ arcmin}$ diameter.

For our analysis we have used the screened event lists from the rev1 processing of the data sets available on the GSFC ASCA archive (for a detailed description of the rev1 processing see the GSFC ASCA Data Reduction Guide, published by GSFC.) The ASCA data were reduced using the FTOOLS software (version 3.6) issued by GSFC, from within the XSELECT environment (version 1.3). Further data-cleaning procedures as recommended in the ASCA Data Reduction Guide, including appropriate grade selection, gain corrections and manual screening based on the individual instrument light curves, were followed. A summary of the ASCA observations, including the individual exposure times after all screening procedures were carried out, is provided in Table 1.

Spectra were extracted from all four ASCA detectors (except in those few cases where the S1 data were lost due to saturation problems caused by flickering pixels in the CCDs). The spectra were extracted from circular regions, centred on the peaks of the X-ray emission. For the SIS data, the radii of the regions used were selected to minimize the number of chip boundaries crossed (thereby minimizing the systematic uncertainties introduced by such crossings) whilst covering as large a region of the clusters as possible. Data from the regions between the chips were masked out and excluded. The final extraction radii for the SIS data are summarized in Table 2. Also included in that Table are the chip modes used in the observations (whether 1,2 or 4 chip mode) and the number of chips from which the extracted data were drawn. For the GIS data a constant extraction radius of 6 arcmin was used. [We note that for Abell 2142, the 2 arcmin (3 arcmin) radius region surrounding the X-ray bright Seyfert-1 galaxy 1556+274 (offset by ~ 4 arcmin from the X-ray centre of the cluster) was masked out and excluded from the analysis of the SIS (GIS) data.]

For the GIS observations, and SIS observations of clusters in regions of low Galactic column density ($N_{\text{H}} \lesssim 5 \times 10^{20} \text{ atom cm}^{-2}$), background subtraction was carried out using the ‘blank sky’ observations of high Galactic latitude fields compiled during the performance verification stage of the ASCA mission. For such data sets, the blank-sky observations provide a reasonable representation of the cosmic and instrumental backgrounds in the detectors. The background data were screened and grade selected in the same manner as the target observations and background spectra were extracted from the same regions of the detectors as the cluster spectra. For the SIS observations of clusters in directions

of higher Galactic column density, background spectra were extracted from regions of the chips that were relatively free from foreground cluster emission.

For the SIS data, response matrices were generated using the FTOOLS SISRMG software. Where the spectra covered more than one chip, response matrices were created for each chip, which were then combined to form a counts-weighted mean matrix. For the GIS analysis, the response matrices issued by GSFC on 1995 March 6 were used.

2.3 The ROSAT observations

The ROSAT HRI observations were carried out between 1991 November and 1995 June. The HRI provides a ~ 5 arcsec (FWHM) X-ray imaging facility covering a $\sim 40 \times 40$ arcmin 2 field of view (David *et al.* 1996). Reduction of the data was carried out with the Starlink ASTERIX package. X-ray images were created on a 2×2 arcsec 2 pixel scale, from which centres for the cluster X-ray emission were determined. Where more than one observation of a source was made, a mosaic was constructed from the individual observations. For the cooling flow and intermediate clusters, the X-ray centres were identified from the peaks of the X-ray surface brightness distributions (which are easily determined from the HRI images). For the non-cooling flow clusters, the X-ray emission is not as sharply-peaked and for these systems we have identified the X-ray centres with the results from iterative determinations of the centroids within a circular aperture of fixed radius. For Abell 665, 2163 and AC114 a 1 arcminute radius aperture was used. For Abell 2744, 773, 2218 and 2219 a 2 arcmin aperture was adopted, and for Abell 520 a 3 arcmin aperture was used. For two of the clusters included in the sample, Abell 665 and 1413, ROSAT HRI images were not available at the time of writing and for these clusters PSPC imaging data have been used instead. A summary of the ROSAT observations and the X-ray centers for the clusters is given in Table 3.

2.4 Classification of clusters as cooling flow (CF) and non-cooling flow (NCF) systems

For the purposes of this paper, we have classified the clusters into subsamples of cooling-flow (hereafter CF) and non-cooling flow (NCF) systems. CFs are those clusters for which the upper (90 percentile) limit to the central cooling time, as determined from the deprojection analysis of the ROSAT HRI X-ray images (Section 4), is less than 10^{10} yr. (The ‘central’ cooling time is the mean cooling time of the cluster gas in the innermost bin included in the deprojection analysis, which is of variable size. The use of a fixed physical size of 100 kpc for the central bin leads to similar results; Section 4.) Using this simple classification scheme we identify 21 CFs and 9 NCFs in our sample. The mean redshift for the subsamples of both CF and NCF clusters is $\bar{z} = 0.21$. The fraction of CFs in our sample is 70 per cent, the same as that determined by Peres *et al.* (1998) from a study of a larger, flux-limited sample of clusters (primarily at lower redshift; $\bar{z} = 0.056$) using a similar classification scheme.

3 SPECTRAL ANALYSIS OF THE ASCA DATA

3.1 The spectral models

The modeling of the X-ray spectra has been carried out using the XSPEC spectral fitting package (version 9.0; Arnaud 1996). For the SIS data, only counts in pulse height analyser (PHA) channels corresponding to energies between 0.6 and 10.0 keV were included in the analysis (the energy range over which the calibration of the SIS instruments is best-understood). For the GIS data only counts in the energy range 1.0 – 10.0 keV were used. The spectra were grouped before fitting to ensure a minimum of 20 counts per PHA channel, allowing χ^2 statistics to be used.

The spectra have been modeled using the plasma codes of Kaastra & Mewe (1993; incorporating the Fe L calculations of Liedahl, Osterheld & Goldstein 1995, in XSPEC version 9.0) and the photoelectric absorption models of Balucinska-Church & McCammon (1992). The data from all four ASCA detectors were analysed simultaneously (except where the S1 data were lost due to chip saturation problems) with the fit parameters linked to take the same values across the data sets. The exceptions to this were the emission measures of the ambient cluster gas in the four detectors which, due to the different extraction radii used and residual uncertainties in the flux calibration of the instruments, were allowed to fit independently.

The spectra were examined with a series of spectral models. Model A, consisted of an isothermal plasma in collisional equilibrium, at the optically-determined redshift for the cluster, and absorbed by the nominal Galactic column density (Dickey & Lockman 1990). The free parameters in this model were the temperature (kT) and metallicity (Z) of the plasma and the emission measures in the four detectors. (The metallicities are measured relative to the solar values of Anders & Grevesse (1989), with the different elements assumed to be present in their solar ratios.) The second model, model B, was the same as model A but with the absorbing column density (N_{H}) also included as a free parameter in the fits. The third model, model C, was the same as model A but with an additional component explicitly accounting for the emission from the cooling flows. The material in the cooling flows is assumed to cool at constant pressure from the ambient cluster temperature, following the prescription of Johnstone *et al.* (1992). The normalization of the cooling-flow component was parameterized in terms of a mass deposition rate, \dot{M}_{S} , which was a free parameter in the fits. The mass deposition rate is linked to take the same value in all four detectors, scaled by a normalization factor proportional to the total flux measured in that detector. The metallicity of the cooling gas was assumed to be equal to that of the ambient ICM. The emission from the cooling flows was also assumed to be absorbed by an intrinsic column density, ΔN_{H} , of cold gas which was a further free parameter in the fits. The abundances of metals in the absorbing material were fixed to their solar values (Anders & Grevesse 1989) although the effects of varying these values were examined. Finally, a fourth spectral model, model D, was examined which was similar to model C but with the constant-pressure cooling flow replaced with a second isothermal emission component. The temperature and normalization of this second emission component were included as free parameters in the fits. (As with model C, the normalizations were linked to the same value in all four detec-

tors, scaled by the appropriate normalization factors.) The second emission component was also assumed to be intrinsically absorbed by a column density of cold gas, ΔN_{H} , which was a free parameter in the fits. The metallicities of the two emission components were linked to take the same values.

Fig. 1 shows the ASCA data and best-fitting spectral models for four of the clusters in the sample; Abell 1704, 2029, 2204 and 2219. Table 4 summarizes the fit results for all of the clusters using the four spectral models. For each cluster we list the best-fitting parameter values and 90 per cent ($\Delta\chi^2 = 2.71$) confidence limits. The mass deposition rates (M_{S}), 2–10 keV X-ray luminosities (L_{X}) and bolometric luminosities (L_{Bol}) are the values measured in the G3 detector. Note that for the clusters at relatively low redshifts ($z < 0.1$), we have corrected the L_{X} and L_{Bol} values for the emission arising at radii > 6 arcmin by scaling from the David *et al.* (1993) results, which were based on GINGA and Einstein MPC observations.

3.2 The goodness-of-fit

Table 5 summarizes the goodness-of-fit measurements obtained with the different spectral models. The tabulated results are the probabilities of exceeding the χ^2 values obtained, assuming in each case that the model correctly describes the spectral properties of the clusters. Goodness-of-fit values $< 10^{-2}$ may be regarded as indicating a formally unacceptable fit to the data.

The results from the spectral analysis show that model A (the isothermal model with the absorbing column density fixed at the nominal Galactic value) provides a reasonable description of most (21/30) of the clusters. However, model A fails significantly for the massive CF clusters Abell 1068, 1795, 2029 and 2204. The significance of the improvements to the fits obtained with spectral model B over model A have been evaluated using the F-test for the introduction of an additional free parameter (Bevington 1969). These significances are listed in Column 6 of Table 5. We see that the improvements obtained when including the column density as a free parameter in the fits with the isothermal models are significant at ≥ 90 per cent confidence for 23 of the 30 clusters (and would also be highly significant for Abell 478 if the nominal Dickey & Lockman 1990 value for the Galactic column density, rather than the X-ray value determined by Allen & Fabian 1997 were used in model A). Model B provides a statistically acceptable fit for 27 of the 30 clusters.

The results on the goodness-of-fit determined with spectral models C and D are summarized in columns 4 and 5 of Table 5. The only clusters that these models do not adequately describe are the two nearest, brightest systems; Abell 1795 and Abell 2029. Spectral models C and D include an absorption component acting on the entire cluster emission which is normalized to the appropriate Galactic column densities determined from HI studies (Dickey & Lockman 1990). We have examined the significance of the improvements to the fits obtained when allowing the Galactic column density to also be a free parameter in the fits with these models. The fits were not significantly improved for any of the clusters except PKS0745-191, for which the Galactic column density is most uncertain. (The Galactic column density to PKS0745-191 varies between 3.2 and 4.4×10^{21} atom cm $^{-2}$ in the surrounding regions studied by Dickey

& Lockman 1990). We find $\Delta\chi^2 = 7.9$ with model C and $\Delta\chi^2 = 20.2$ with model D for PKS0745-191 (indicating improvements significant at > 99 per cent confidence) when allowing the Galactic column density to be free. The preferred value for the Galactic column density for this cluster from the ASCA data is $\sim 3.5 \times 10^{21}$ atom cm $^{-2}$. For Abell 1795, we also find a marginal improvement to the fits with models C and D when allowing the Galactic column density to be a free parameter ($\Delta\chi^2 = 4.5$ with Model C and $\Delta\chi^2 = 5.4$ for model D, which is significant at the 96.5 and 98 per cent level, respectively) with a preferred value of $\leq 8 \times 10^{19}$ atom cm $^{-2}$. The agreement between the Galactic column densities inferred from the 21 cm and X-ray data for most of the clusters with spectral models C and D provides further support for the validity of these models.

3.3 The requirement for multiphase models

The statistical improvements obtained by introducing an additional emission component into the fits with the single-temperature model (model B) are summarized in Columns 7 and 8 of Table 5. We list the results obtained for both cases, where the extra emission component is modeled as a cooling flow (for the CF systems only) or a second isothermal emission component. (Essentially we use spectral models C and D, but also include the Galactic column density as a free parameter in the fits so as to permit a direct comparison with the goodness of fit measured with spectral model B). The significance of the improvements to the fits obtained with the multiphase models with respect to model B have been quantified using an F-test for the introduction of 2 or 3 extra parameters (for models C and D respectively). We find that the improvements with model D are significant at ≥ 90 per cent confidence for 21 of the 30 clusters. The only clusters for which we find no significant improvement with the introduction of a second emission component are the NCF clusters Abell 520, 773, 2218 and AC114, and the more distant and/or less-luminous CF clusters Abell 963, MS1358.4+6245, MS1455.0+2232, MS2137.3-2353 and Abell 2390, which have amongst the lowest numbers of counts in their ASCA spectra. For the CF clusters (the only clusters to which model C was applied) the improvements obtained with the cooling-flow model over model B are significant at ≥ 90 per cent confidence in 13 of 21 systems, with again those CF clusters with the lowest numbers of total counts in their ASCA spectra exhibiting the least-significant improvements.

We thus find that most CF clusters, and a number of NCF systems (in general those systems with the best signal-to-noise ratios in their ASCA spectra) exhibit significant improvements to their fits with the use of multiphase, over single-phase, models. These improvements generally indicate the presence of emission from material cooler than the mean cluster temperatures (see Table 4). For the CF clusters, this can be naturally understood as being due to emission associated with the cooling flows. For the NCF clusters, the improvements to the fits obtained with model D are likely to reflect the presence of merging subclusters with lower virial temperatures. This is supported by optical, radio and X-ray imaging (*e.g.* Edge *et al.* 1992; Buote & Tsai 1996; Markevitch 1996; Feretti, Giovannini & Böhringer 1997; Rizza *et al.* 1998) and gravitational lensing studies (*e.g.* Kneib *et al.*

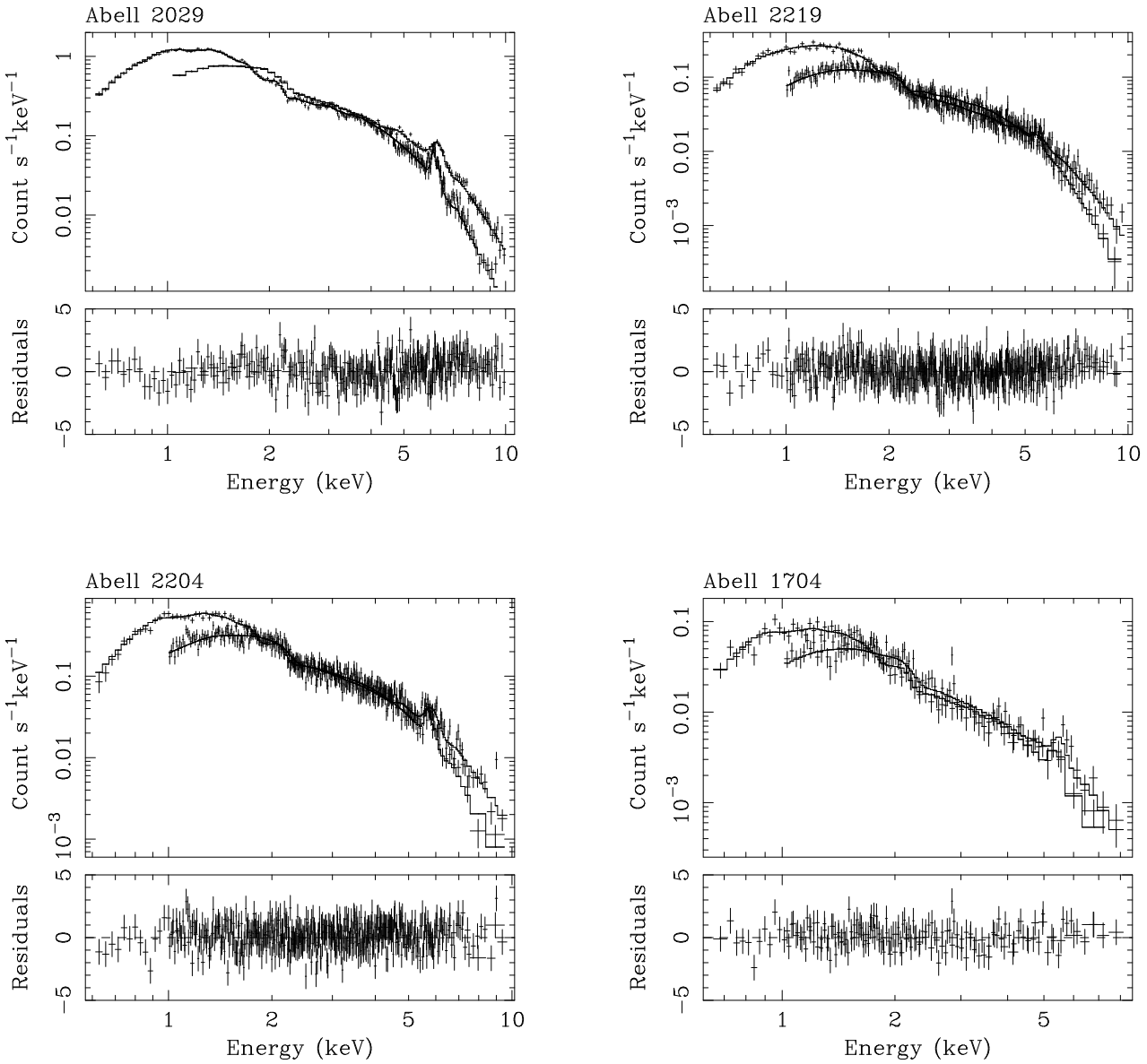


Figure 1. (Upper panels) The ASCA data and best-fitting models and (lower panels) residuals to the fits (in units of χ^2) for a representative subsample of the clusters included in the study. Clockwise, from top left, we show Abell 2029, 2219, 1704 and 2204. For the 3 CF clusters (Abell 2029, 2204 and 1704), the results determined with spectral model C are shown. For the NCF cluster, Abell 2219, spectral model B is shown. For clarity, only the S0 and G3 data are plotted. The figure illustrates the range in quality of the ASCA data included in the study.

1995; Smail *et al.* 1995, 1997; Squires *et al.* 1997; Allen 1998) of the NCF clusters, which show that these systems typically exhibit complex morphologies and centroid shifts indicative of merger events.

3.4 Two-temperature versus cooling-flow models

The results in Table 4 show that spectral model D typically provides at least as good a fit to the ASCA spectra for the CF clusters as the cooling-flow model (model C). This has sometimes been taken to indicate that the X-ray gas in these

systems is distinctly two-phase, with the cooler phase being due to the dominant cluster galaxy (*e.g.* Makishima 1997; Ikebe *et al.* 1999). However, when interpreting these results it is important to recall that the two-temperature model provides a more flexible fitting parameterization, with an extra degree of freedom, when applied to ASCA observations. Simulated cooling-flow spectra constructed with spectral model C, including plausible levels of intrinsic absorption (Section 6) and observed at the spectral resolution and signal-to-noise levels typical of ASCA observations, are invariably well-described by two-temperature models. This is

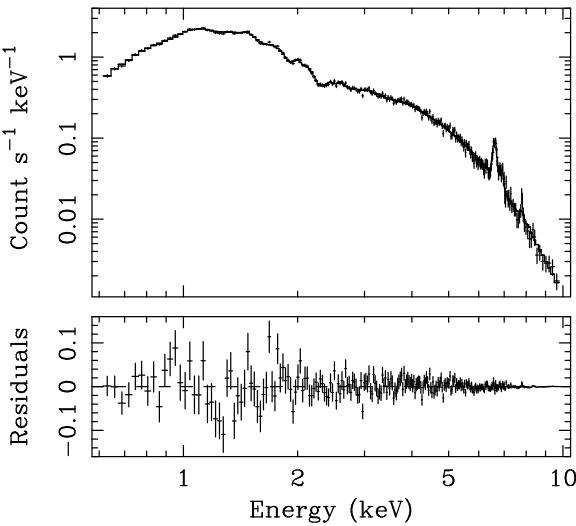


Figure 2. (Upper panel) Simulated ASCA SIS spectrum of a 7 keV cluster with a metallicity of $0.4Z_{\odot}$ and a cooling flow, intrinsically absorbed by a column density of $4 \times 10^{21} \text{ atom cm}^{-2}$, accounting for 30 per cent of the total 2 – 10 keV flux. A count rate of 1 ct s^{-1} , an exposure time of 40ks and a Galactic column density of $10^{20} \text{ atom cm}^{-2}$ have been assumed. The best-fitting two-temperature model (which provides a χ^2 of 263 for 245 degrees of freedom) is overlaid. The best-fit parameters are $kT_1 = 6.7 \pm 0.4 \text{ keV}$, $kT_2 = 1.4 \pm 0.2 \text{ keV}$, $Z = 0.41 \pm 0.04Z_{\odot}$, with an intrinsic column density acting on the cooler component of $7.6 \pm 1.8 \times 10^{21} \text{ atom cm}^{-2}$. (Lower panel) The residuals to the fit in units of $\text{count s}^{-1} \text{ keV}^{-1}$.

illustrated in Fig. 2 where we show a simulated ASCA SIS spectrum for a 7 keV cluster with a metallicity of $0.4Z_{\odot}$, containing a cooling flow (intrinsically absorbed by a column density of $4 \times 10^{21} \text{ atom cm}^{-2}$) accounting for 30 per cent of the total 2 – 10 keV flux. A count rate of 1 ct s^{-1} , an exposure time of 40ks and a Galactic column density of $10^{20} \text{ atom cm}^{-2}$ have been assumed. Overlaid, we show the best-fitting two-temperature model, which provides a good fit to the simulated data.

Thus, even in the case where the constant-pressure cooling flow model provides an exact description of the data (*i.e.* in the simulations), the two-temperature model provides a similarly good fit. In a real cluster, where spectral model C will undoubtedly over-simplify the true situation, the more flexible two-temperature model (model D) is likely to provide a better match to the observations. Thus, our finding that spectral model D often provides a better fit to the observed cluster spectra than model C, only shows that the constant pressure cooling flow model over-simplifies the true spectra of the cooling flows in the clusters (see also Section 6.4). We note that such tendencies would be enhanced by the presence of additional cool components in the spectra, for example due to temperature gradients at large radii (*e.g.* Markevitch *et al.* 1998). Finally, we note that the very high luminosities associated with the cool emission components in clusters like RXJ1347.5-1145 (with $L_{\text{cool}} \sim$ a few $10^{45} \text{ erg s}^{-1}$) are difficult to explain with models in which

the cool emission is due to the interstellar medium of the central cluster galaxies.

4 DEPROJECTION ANALYSIS OF THE X-RAY IMAGES

4.1 Method and primary results

The analysis of the HRI imaging data has been carried out using an extensively updated version of the deprojection code of Fabian *et al.* (1981). Azimuthally-averaged X-ray surface brightness profiles were determined for each cluster from the HRI images. These profiles were background-subtracted, corrected for telescope vignetting and re-binned to provide sufficient counts in each annulus to allow the analysis to be extended to radii of at least 500 kpc. (Bin sizes of 8–24 arcsec were used.)

With the X-ray surface brightness profiles as the primary input, and under assumptions of spherical symmetry and hydrostatic equilibrium, the deprojection technique can be used to study the basic properties of the intracluster gas (temperature, density, pressure, cooling rate) as a function of radius. The deprojection code uses a monte-carlo method to determine the statistical uncertainties on the results and incorporates the appropriate HRI spectral response matrix issued by GSFC. The cluster metallicities were fixed at the values determined from the spectral analysis (Table 4). The absorbing column densities were fixed at the appropriate Galactic values (Table 1).

The deprojection code requires the total mass profiles for the clusters (which define the pressure profiles) to be specified. We have iteratively determined the mass profiles that result in deprojected temperature profiles (which approximate the mass-weighted temperature profiles in the clusters) that are isothermal within the regions probed by the HRI data (the central 0.5 – 1 Mpc) and which are consistent with the spectrally-determined temperatures (Section 3). The assumption of approximately isothermal mass-weighted temperature profiles in the central regions of the clusters is supported by the following evidence: firstly, ASCA observations of nearby cooling flows show that in the central regions of these systems the gas is multiphase, but that the bulk of the X-ray gas there has a temperature close to the cluster mean (*e.g.* Fabian *et al.* 1994b; Fukazawa *et al.* 1994; Matsumoto *et al.* 1996; Ikebe *et al.* 1999). Secondly, combined X-ray and gravitational lensing studies of CF clusters (*e.g.* Allen 1998) show that approximately isothermal mass-weighted temperature profiles in the cores of such clusters lead to excellent agreement between their X-ray and gravitational-lensing masses. Thirdly, the use of approximately constant mass-weighted temperature profiles implies a more plausible range of initial density inhomogeneities in the clusters than would be the case if the temperature profiles decreased within their cores (Thomas, Fabian & Nulsen 1987). Finally, the use of approximately isothermal mass-weighted temperature profiles in the deprojection analyses leads to independent determinations of the mass deposition profiles in the cooling flows, from the X-ray spectra and imaging data, in excellent agreement with each other (*e.g.* Allen & Fabian 1997). We note that the assumption of a constant mass-weighted deprojected temperature profile is consistent with measurements of a decreasing emission-weighted

temperatures in the cores of many CF clusters (e.g. Waxman & Miralda-Escudé 1995).

The mass profiles for the clusters were parameterized as isothermal spheres (Equation 4-125 of Binney & Tremaine 1987) with adjustable core radii (r_c) and velocity dispersions (σ). The core radii were adjusted until the temperature profiles determined from the deprojection code became isothermal. The velocity dispersions were then adjusted until the temperatures determined from the deprojection code came into agreement with the spectrally-determined values. Errors on the velocity dispersions are the range of values that result in isothermal deprojected temperature profiles that are consistent, at the 90 per cent confidence limit, with the spectrally-determined temperature results. Estimates of the thermal gas pressure in the outermost radial bins used in the analysis are also required by the deprojection code and were determined iteratively. (The uncertainties on the outer pressure estimates do not significantly affect the results presented here.) Although the deprojection method of Fabian *et al.* (1981) is essentially a single-phase technique, we note that it produces results in good agreement with more detailed multiphase treatments (Thomas, Fabian & Nulsen 1987) and, due to its simple applicability at large radii in clusters, is better-suited to the present project.

The mass distributions determined from the deprojection analysis are summarized in columns 3 and 4 of Table 6. These simple parameterizations permit direct comparisons with independent mass constraints from gravitational lensing and dynamical studies (e.g. Allen 1998). We note that for a few of the clusters (primarily the brightest CFs with the best data) the single-component mass models cannot adequately satisfy the requirement for approximately isothermal deprojected temperatures profiles and for these systems a significantly better match was obtained by introducing a second ‘linear’ mass component, truncated at a specified outer radius. The clusters requiring the additional mass components were Abell 586 ($2 \times 10^{11} M_\odot \text{kpc}^{-1}$ within the central 20 kpc), Abell 2029 ($3 \times 10^{11} M_\odot \text{kpc}^{-1}$ within the central 20 kpc), Abell 2219 ($10^{11} M_\odot \text{kpc}^{-1}$ within the central 30 kpc), Abell 478 ($4 \times 10^{11} M_\odot \text{kpc}^{-1}$ within the central 20 kpc and an adjustment of the cluster parameters to $\sigma = 840^{+80}_{-60} \text{ km s}^{-1}$ and $r_c = 100 \text{ kpc}$) and Abell 1795 ($10^{11} M_\odot \text{kpc}^{-1}$ within the central 20 kpc, and an adjustment of the cluster parameters to $\sigma = 720^{+20}_{-20} \text{ km s}^{-1}$ and $r_c = 60 \text{ kpc}$).

The core radii of the mass distributions determined from the deprojection analysis are similar to the values measured from simple ‘ β -model’ fits to the X-ray surface brightness profiles (e.g. Cavaliere & Fusco-Femiano 1976, 1978). It is well known that the β -model does not provide a good match to the X-ray surface brightness profiles of the brightest CF clusters when their central regions are included in the analysis (e.g. Jones & Forman 1984). However, where β -models are used to estimate the mass core radii in CF clusters, the central regions of these clusters should not simply be excised from the fits. The central surface brightness peaks in CF clusters trace the presence of sharp central density rises in these systems and are not only the result of excess emission due to cooling gas. (It is the high central densities that lead to the high cooling rates.) Although fully accounting for the effects of cooling on the central density measurements is difficult with current data, simply excising

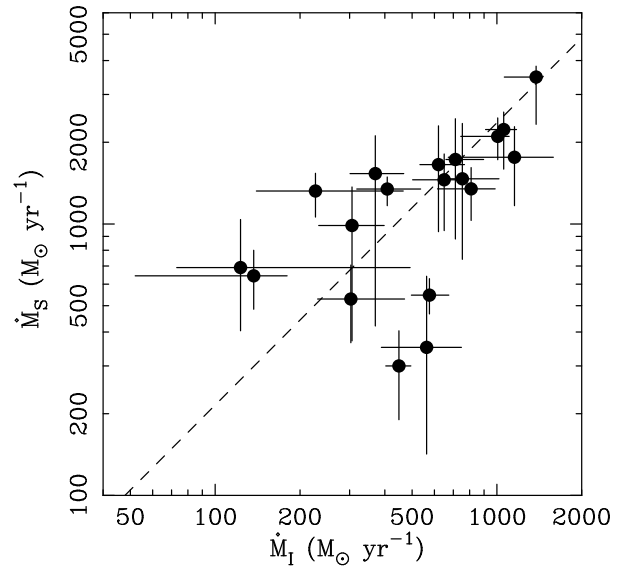


Figure 3. The mass deposition rates determined from the ASCA spectra (M_S) versus the values measured from the deprojection analysis of the ROSAT HRI imaging data (M_I). The dashed line is the best-fitting power-law model. No correction for the effects of intrinsic absorption on the deprojection results has been made.

the inner regions of the clusters can lead to overestimates of the mass core radii and corresponding underestimates of the central gas and total mass densities.

The basic results on the cooling flows from the deprojection analysis are summarized in columns 5–8 of Table 6. For those clusters in common, the results obtained are generally in good agreement with values reported from previous works (e.g. Edge *et al.* 1992, White *et al.* 1997; Peres *et al.* 1998).

5 THE MASS DEPOSITION RATES FROM THE COOLING FLOWS

5.1 Comparison of the spectral and imaging results

The spectral and image deprojection analyses discussed in Sections 3 and 4 provide essentially independent estimates of the mass deposition rates in the clusters. A comparison of the results obtained from these analyses therefore provides a test of the validity of the cooling flow model.

The deprojection method describes the X-ray emission from a cluster as arising from a series of concentric spherical shells. The luminosity in a particular shell, j , may be written as the sum of four components (Arnaud 1988).

$$L_j = \Delta \dot{M}_j H_j + \Delta \dot{M}_j \Delta \Phi_j + \left[\sum_{i=1}^{j-1} \Delta \dot{M}_i (\Delta \Phi_j + \Delta H_j) \right], \quad (1)$$

where $\Delta \dot{M}_j$ is the mass deposited in shell j , H_j is the enthalpy of the gas in shell j , and $\Delta \Phi_j$ is the gravitational energy released in crossing that shell. $\sum_{i=1}^{j-1} \Delta \dot{M}_i$ is the mass flow rate through shell j , and ΔH_j the change of enthalpy

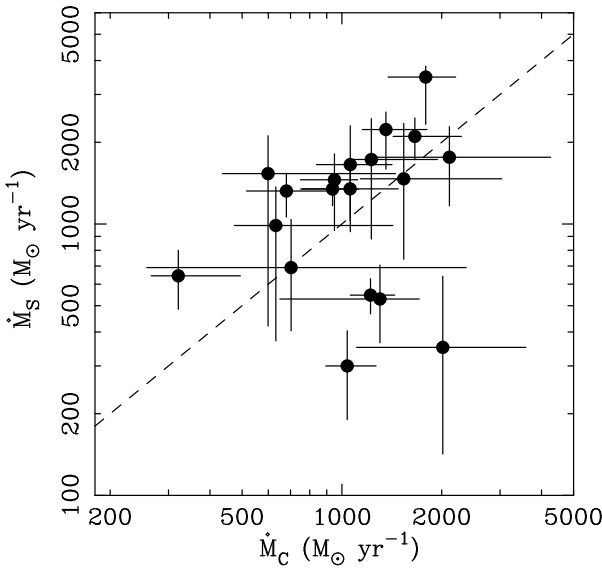


Figure 4. The mass deposition rates determined from the ASCA spectra (\dot{M}_S) versus the values measured from the deprojection analysis, corrected for the effects of intrinsic absorption due to cold gas (\dot{M}_C). The dashed line indicates equality between the values.

of the gas as it moves through that shell. The first term in equation 1 thus accounts for the enthalpy of the gas deposited in shell j . The second term is the gravitational work done on the gas deposited in shell j . The third and fourth terms respectively account for the gravitational work done on material flowing through shell j to interior radii, and the enthalpy released by that material as it passes through the shell.

In any particular shell, the densest material in the cooling flow is assumed to cool out and be deposited. Since the cooling time of this material will be short compared to the flow time, the cooling can be assumed to take place at a fixed radius. Thus, the luminosity contributed by the first term in equation 1 should have a spectrum that can be approximated by gas cooling at constant pressure from the ambient cluster temperature *i.e.* the same spectrum as the cooling component incorporated into the spectral analysis with model C (Section 3).

For the bulk of the material continuing to flow inwards towards the cluster centre, the cooling via X-ray emission is assumed to be offset by the gravitational work done on the gas as it moves inwards. The emission accounted for in the second and third terms of equation 1 should therefore have a spectrum that can be approximated by an isothermal plasma at the appropriate ambient temperature for the cluster *i.e.* the spectrum of the isothermal emission component in model C. Since the mass-weighted temperature profiles in the clusters are assumed to remain approximately isothermal with radius, the luminosity contributed by the fourth term of equation 1 should be negligible.

The mass deposition rates, \dot{M}_I , listed in Table 6 are the mass flow rates ($\sum_{i=1}^{j-1} \Delta \dot{M}_i$) determined from the deprojection analysis, at the point where the mean cooling time

of the cluster gas first exceeds the Hubble time (1.3×10^{10} yr). Thus, if the cooling flow model is correct, and the cooling flows have been undisturbed for a significant fraction of a Hubble time, the mass deposition rates determined from the deprojection analysis should be similar to those measured independently from the spectral data.

Fig. 3 shows the mass deposition rates determined from the spectral analysis (\dot{M}_S) versus the image deprojection results (\dot{M}_I), for those clusters for which both quantities have been measured. We see that the results exhibit an approximately linear correlation; a fit to the data with a power-law model of the form $\dot{M}_S = P \dot{M}_I^Q$, using the Akritas & Bershady (1996) bisector modification of the ordinary least-squares statistic, gives a best-fitting power-law slope of 1.0 ± 0.2 (where the error is the standard deviation determined by bootstrap re-sampling), although the spectrally-determined mass deposition rates typically exceed the deprojection results by a factor of 2–3. However, the spectral analysis presented in Section 3 also requires that the cooling gas is intrinsically absorbed by equivalent hydrogen column densities of, typically, a few 10^{21} atom cm $^{-2}$ (model C). The mass deposition rates determined from the deprojection analysis must therefore also be corrected for the effects of this absorbing material.

The corrections for the effects of intrinsic absorption on the deprojection results have been carried out by re-running the deprojection analysis with the absorbing column densities set to the total values determined with spectral model C. We assume that the absorption is due to cold gas with solar metallicity. If, however, the intrinsic absorption were instead due to dust, a possibility examined in more detail in Section 7, then the required correction factors would likely be reduced by a few tens of per cent. (The introduction of a simple OIK absorption edge at $E \sim 0.54$ keV, such as might be associated with oxygen-rich, silicate dust grains, generally provides as good a description of the intrinsic absorption detected in the 0.6–10.0 keV ASCA spectra as a cold, gaseous absorber.) Since the intrinsic column densities measured with model C are redshifted quantities, we set the total column densities used in the revised deprojection analysis, which assumes zero redshift for the absorber, to be $N_H + \Delta N_H / (1 + z)^3$, where N_H is the Galactic column density. The absorption-corrected mass deposition rates (\dot{M}_C) so determined are summarized in Table 7. Fig. 4 compares the spectrally-determined mass deposition rates with the absorption-corrected deprojected values. We see that once the presence of intrinsic absorption has been accounted for in a consistent manner in the imaging and spectral analyses, the results on the mass deposition rates in the clusters show good agreement.

5.2 The fraction of flux from the cooling flows

Table 8 lists the fractions of the total 2–10 keV X-ray fluxes from the CF clusters associated with cooling gas, as determined with spectral model C. The results range from ~ 10 per cent for systems like Abell 1689 and 2142 to > 30 per cent for Zwicky 3146, Abell 1068, RXJ1347-1145 and Abell 2204. Such a range of measurements is consistent with the results of Peres *et al.* (1998), from a deprojection analysis of a flux-limited sample of the brightest clusters known.

The fraction of the X-ray flux from a cluster due to it's

cooling flow can be expected to increase with the age of the flow. It is therefore likely that the cooling flows in Abell 1689 and 2142 are younger than those in Abell 2204 and Zwicky 3146. We note that the X-ray data are not, in general, of sufficient quality to place firm constraints on the ages of the cooling flows in these clusters (for a discussion of cooling flow age measurements see Allen *et al.* 1999).

It is interesting that the clusters with the largest cooling-flow flux fractions (with the exception of Abell 1413 and 2261) are also amongst the most optically line-luminous cooling flows known (*e.g.* Crawford *et al.* 1999). The production of powerful optical emission lines and associated UV/blue continuum emission is known to be due, at least in part, to the formation of massive stars at the centres of cooling flows (*e.g.* Johnstone, Fabian & Nulsen 1987; Allen 1995; Cardiel *et al.* 1995, 1998; McNamara *et al.* 1996; Voit & Donahue 1997). The results presented here are consistent with the idea that such star formation is typical of undisturbed cooling flows. It is also interesting to note that the clusters with the largest cooling flow flux fractions and most optically line-luminous emission line nebulae also tend to have the shortest cooling times averaged over their central 100 kpc regions, with $\overline{t_{100}} \lesssim 3$ Gyr (see also Peres *et al.* 1998).

6 INTRINSIC X-RAY ABSORPTION IN CLUSTERS

6.1 The measured column densities and model dependency of the results

The equivalent column densities of intrinsic X-ray absorbing material inferred from the spectral analysis are summarized in Table 9. All three of the spectral models incorporating a free-fitting absorption component (models B,C,D) reveal the presence of excess X-ray absorption over and above the nominal Galactic values along the lines of sight to the clusters (Dickey & Lockman 1990), although the measured column densities are sensitive to the spectral model used.

Using the simple isothermal model with free-fitting absorption (model B), we determine a mean excess column density for the whole sample of 30 clusters of $3.8 \pm 3.2 \times 10^{20}$ atom cm $^{-2}$. When we examine the CF and NCF clusters separately, we find that both subsamples exhibit intrinsic absorption, at a similar level on average. For the CF clusters, the mean excess column density measured with spectral model B is $3.5 \pm 3.0 \times 10^{20}$ atom cm $^{-2}$. For the NCF systems, the value is $4.4 \pm 3.9 \times 10^{20}$ atom cm $^{-2}$. The application of a Students t-test (accounting for the possibility of unequal variances in the two distributions; Press *et al.* 1992) shows the mean excess column densities for the CF and NCF clusters, determined with spectral model B, to differ at only the 45 per cent confidence level. The application of a Kolmogorov-Smirnov test shows the two subsamples to be drawn from different parent populations at only the ~ 10 per cent confidence level. Thus, our analysis with spectral model B suggests that intrinsic absorption is not confined to CF clusters.

The results on the column densities are quite different, however, when the more-sophisticated multiphase spectral models are used. As discussed in Section 3, the multiphase models generally provide a better description of the X-ray

properties of the CF clusters (and some of the brighter NCF systems). Using spectral model C, our preferred model for the CF clusters in that it provides a consistent description of the spectral and imaging X-ray data for these systems (Section 5.1), we determine a mean intrinsic column density acting on the cooling-flow components of $3.4 \pm 1.3 \times 10^{21}$ atom cm $^{-2}$. Using the two-temperature spectral model (model D), we determine a mean intrinsic column density acting on the cooler emission components in the CF systems of $6.3 \pm 4.7 \times 10^{21}$ atom cm $^{-2}$. Thus, the intrinsic column densities for the CF clusters measured with the multiphase models (models C and D) are similar and approximately an order of magnitude larger than the values inferred using the single-phase model B. These results demonstrate the need for adopting an appropriate spectral when attempting to measure the column densities of absorbing material in CF clusters. We also note that where spectral model D provided a significant improvement to the fits to the NCF clusters, with respect to model B, the measured column densities acting on the cooler emission components were also significantly larger than the values determined using the single-phase models.

We have also measured the intrinsic column densities in the CF clusters using one further spectral model, referred to in Table 9 as model C'. Model C' is identical to model C except that it assumes that the excess absorption acts on the entire cluster spectrum, rather than just the cooling gas, and that the absorbing material lies at zero redshift. Model C' has been used in a number of previous studies and is included here for comparison purposes. The mean excess column density for the CF clusters determined with spectral model C' is $7.2 \pm 3.9 \times 10^{20}$ atom cm $^{-2}$.

Allen & Fabian (1997) present results from an X-ray colour deprojection study of 18 clusters observed with the ROSAT PSPC. These authors determine intrinsic column densities across the central 30 arcsec (radius) regions of Abell 478, 1795 and 2029, using spectral model C', of 7.40 ± 0.63 , 2.20 ± 0.20 and $0.83 \pm 0.42 \times 10^{20}$ atom cm $^{-2}$, respectively. The results for Abell 478 and Abell 1795 are in excellent agreement with those presented here, although the Allen & Fabian (1997) value for Abell 2029 is ~ 4 times smaller than our result. Abell 2029 is unusual in that it hosts a strong cooling flow without associated optical line emission. This may indicate that the central regions of the cluster have been disrupted (perhaps by a minor merger event or the strong central radio source in this system), complicating the distributions of cooling and absorbing material (*cf.* Section 5.2).

Four of the CF clusters studied here were also examined by White *et al.* (1991), using Einstein Observatory SSS data. These authors measured intrinsic column densities for Abell 478, 1795, 2029 and 2142 (in a 3 arcmin radius circular aperture, using spectral model C') of $1.7^{+0.8}_{-0.7} \times 10^{21}$ atom cm $^{-2}$, $0.8^{+0.3}_{-0.3} \times 10^{21}$ atom cm $^{-2}$, $1.8^{+0.5}_{-0.5} \times 10^{21}$ atom cm $^{-2}$ and $1.3^{+0.3}_{-0.4} \times 10^{21}$ atom cm $^{-2}$, respectively. (The SSS result for Abell 478 has been corrected to account for the different value of Galactic absorption assumed in that study). The intrinsic column densities determined by White *et al.* (1991) are 2–5 times larger than the values measured from the ASCA data.

Allen & Fabian (1997) compared the results from their X-ray colour deprojection study of PSPC data with the

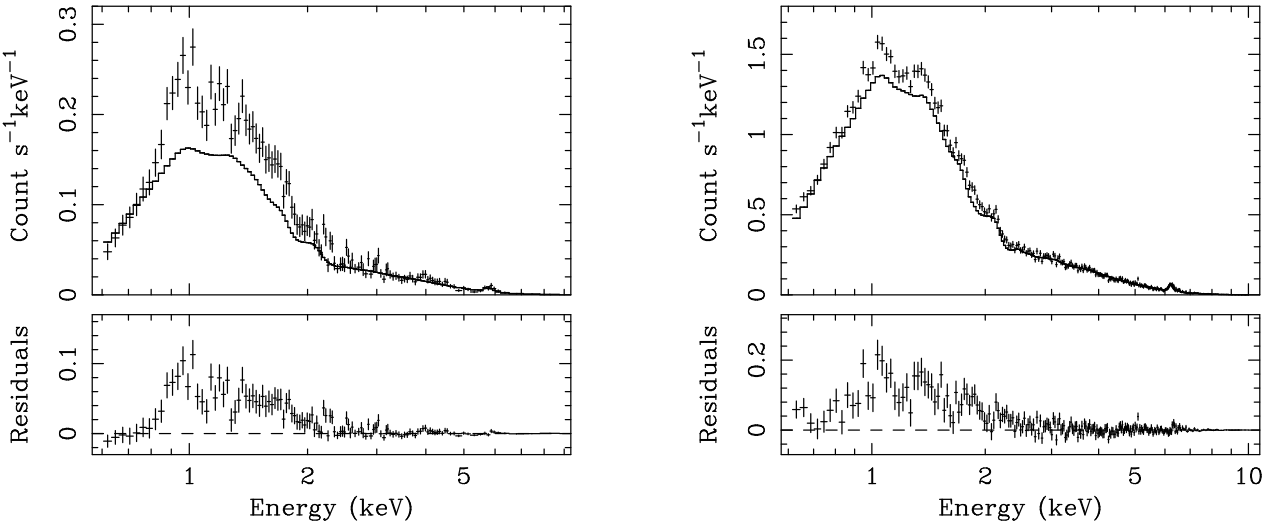


Figure 5. The data, best-fit models and residuals from the fits to the SIS0 spectra for Abell 1068 and 1795 in the energy range 3.0 – 10.0 keV, using spectral model A. The best-fit models have then been extrapolated to cover the full 0.6 – 10.0 keV band. The upper panels show the data and best-fit models. The lower panels show the residuals to the fits. The figures show that the residuals, which can be naturally explained by the introduction of cool emission components with associated intrinsic absorption, take the form of an excess of counts between energies of ~ 0.8 – 2.5 keV.

White *et al.* (1991) SSS analysis and concluded that if the intrinsic absorption were due to cold gas, then agreement between the measured column densities could only be obtained if the covering fraction of the X-ray absorbing material were, in general, $\lesssim 0.5$. We have therefore examined the constraints on the covering fraction, f , that can be obtained from the ASCA data using spectral model C. The results are also listed in Table 9. In all cases we determine a best-fit covering fraction for the intrinsic X-ray absorbing material of unity. For many clusters, covering fractions of < 70 per cent can be firmly ruled out. (The physical significance of these results are further explored in Section 6.4). The results on the covering fractions, and the reasonable agreement of the ASCA and PSPC results for Abell 478 and 1795, suggest that the White *et al.* (1991) results may have systematically over-estimated the intrinsic column densities in clusters by a factor of a few.

Before considering in more detail the possible origin and nature of the absorbing material, it is pertinent to consider whether the intrinsic absorption, inferred to be present using a variety of spectral models, could in fact be an artifact due to an unconsidered emission process in the clusters. Fig. 5 shows the SIS0 spectra for Abell 1068 and 1795, which exhibit two of the clearest absorption signatures. The data between 3.0 and 10.0 keV have been fitted with a single-temperature emission model with Galactic absorption (*i.e.* spectral model A). The residuals to these fits, over the full 0.6 – 10.0 keV band, are shown in the lower panels. We see that the residuals, which can be naturally explained by the introduction of cool emission components with associated intrinsic absorption (using spectral models C and D), take the form of a large excess of counts between ~ 0.8 – 2.5 keV. We therefore include the caveat that if some extra emission

process which can account for such residuals in the X-ray spectra were identified, then the requirement for intrinsic absorption from the X-ray data would be greatly diminished. Finally, we note that the fits with spectral Model A over the restricted 3.0 – 10.0 energy range lead to determinations of the cluster temperatures for Abell 1068 and 1795 of $6.1^{+2.6}_{-1.6}$ and $6.1^{+0.5}_{-0.4}$ keV, respectively, in excellent agreement with the results obtained for the full data sets with spectral model C.

6.2 The mass of absorbing material

The results presented in Section 6.1 show that the cooling flows in our sample are typically intrinsically absorbed by equivalent hydrogen column densities of a few $\times 10^{21}$ atom cm^{-2} (taking spectral model C as our preferred model). Assuming, in the first case, that this absorption is due to cold gas with solar metallicity, the mass of absorbing gas, M_{abs} , within a radius, r_{abs} , may be approximated as

$$M_{\text{abs}} \sim 3.2 \times 10^7 r_{\text{abs}}^2 \Delta N_{\text{H}} M_{\odot}, \quad (2)$$

where r_{abs} is in units of kpc and ΔN_{H} in 10^{21} atom cm^{-2} . For metallicities of $0.4Z_{\odot}$ in the absorbing gas (the mean emission-weighted value for the X-ray emitting gas in the CF clusters; Allen & Fabian 1998b) the implied masses are a factor ~ 2 larger. For zero metallicity these masses are a factor ~ 3 times larger than the values given by equation 2. (The scaling factors for different metallicities in the absorbing material have determined from spectral simulations using the XSPEC code.)

We have adopted r_{abs} as the radius where the cooling time of the cluster gas first exceeds 5×10^9 yr in the clusters

(a plausible age for the cooling flows in most of the CF systems). These radii, and the masses of absorbing gas implied by equation 2 (using the column densities determined with spectral model C) for both solar metallicity and $Z = 0.4Z_{\odot}$, are listed in columns 2 – 4 of Table 10.

The observed masses of absorbing material may be compared to the masses expected to have been accumulated by the cooling flows (M_{acc}) within the same radii over the past 5×10^9 yr. Assuming that from time $t = 0$ to $t = 5 \times 10^9$ yr, the integrated mass deposition rate within radius r_{abs} increases approximately linearly with time, the total mass accumulated within radius r_{abs} after 5×10^9 yr is approximately

$$M_{\text{acc}} \sim 2.5\dot{M}(r < r_{\text{abs}}) \times 10^9 \text{ M}_{\odot}. \quad (3)$$

At times $t > 5 \times 10^9$ yr, the mass deposition rate within r_{abs} should remain approximately constant. If instead we assume $\dot{M}(r < r_{\text{abs}})$ to be constant during the first 5 Gyr, the accumulated mass will be twice the value indicated by equation 3. (Exactly how the mass deposition rate within r_{abs} grows with time during the first 5 Gyr is unclear and will depend upon the evolution of the cluster and the detailed properties of the cluster gas.)

The mass deposition rates within radii r_{abs} (corrected for the effects of absorption due to cold gas, as discussed in Section 5.1) and the estimated masses of cooled material accumulated by the cooling flows within these radii over a 5 Gyr period, are summarized in Table 10. Fig. 6 compares the accumulated masses with the masses of absorbing material determined from the spectral data. The agreement between the results is reasonable and is maximized for a metallicity in the absorbing gas of $\sim 0.4 - 0.6Z_{\odot}$ (depending on the growth of the cooling flow over the first 5 Gyr). This supports the idea that the observed X-ray absorption may be due to material accumulated by the cooling flows. We note that if the X-ray absorption in the CF clusters were due to dust rather than cold gas, a possibility examined in more detail in Section 7, then the agreement between the observed and predicted masses of absorbing material shown in Fig. 6 might still be expected to hold if the dust were contained in the material deposited by the cooling flows. In this case, the mass of the absorber calculated with equation 2 would be the mass of cooled gas associated with the dust when it was deposited from the cooling flow. For a Galactic dust to gas ratio, the mass in dust would be ~ 100 times smaller than the associated gas mass.

6.3 The luminosity reprocessed in other wavebands

The luminosities absorbed at X-ray wavelengths must eventually be reprocessed in other wavebands. If the absorbing material is dusty (as is likely to be the case in the central regions of the clusters *e.g.* Voit & Donahue 1995; Fabian, Johnstone & Daines 1994; Allen *et al.* 1995) then the bulk of this reprocessed emission is likely to emerge in the infrared band (*e.g.* Dwek, Rephaeli & Mather 1990). Table 11 summarizes the reprocessed luminosities (*i.e.* the bolometric luminosities absorbed within the clusters) measured with spectral model C. The reprocessed luminosities range from $\sim 2 \times 10^{44}$ erg s $^{-1}$ for Abell 1795 to $\sim 5 \times 10^{45}$ erg s $^{-1}$ for RXJ1347.5-1145, with a mean value of $\sim 10^{45}$ erg s $^{-1}$.

Allen *et al.* (1999) report detections of spatially extended 100 μm emission coincident with the X-ray centroids in the nearby Centaurus cluster and Abell 2199. The infrared fluxes from those clusters were also shown to be in good agreement with the predicted values due to reprocessed X-ray emission from their cooling flows. We have also used the IPAC SCANPI software and archival IRAS data to measure the 60 and 100 μm fluxes within a four arcmin (radius) aperture centred on the X-ray centroids for the clusters in the present sample. (The medians of the co-added SCANPI results were used.) The results are listed in Table 11. The error bars associated with the measured fluxes are the root-mean-square deviations in the residuals, external to the source extraction regions, after baseline subtraction. Where no detection was made, an upper limit equal to three times the r.m.s. deviation in the residuals is listed. Where a detection was made, we also list the in-scan separations (in arcmin) between the peak of the 100 μm emission (or the 60 μm emission in the case of Abell 1835) and the X-ray centre.

Two of the clusters in our sample, IRAS 09104+4109 and Abell 1068 have known infrared point sources coincident with their X-ray centroids (Kleinmann *et al.* 1988; Moshir *et al.* 1989). The presence of these sources is confirmed by our analysis. The 60 and 100 μm data for Abell 1704 and 60 μm data for Abell 1835 also suggest the presence of unresolved sources, coincident with the X-ray centroids for the clusters. Abell 478 and Zwicky 3146 have 100 μm emission originating from close to their X-ray centroids, which appears spatially extended, although the infrared flux from Abell 478 is probably contaminated by Galactic cirrus. The data for Abell 2142, 2204, 2261 and 2390 also provide significant detections within the four arcmin (radius) source apertures, although the peaks of the infrared emission from these systems are spatially offset from their X-ray centroids, suggesting that the detected flux is likely to originate, at least in part, from some other source.

Several of the clusters included in our study (Abell 586, 963, 1413, 1795, 2029, 2142 and PKS0745-191) have previously been studied at infrared wavelengths, using IRAS data, by Wise *et al.* (1993) and/or Cox, Bregman & Schombert (1995). These authors also report no clear detections of infrared emission from these sources. Edge *et al.* (1999) report measurements of 60 μm emission from Abell 1835 and 60 and 100 μm emission from Abell 2390, using a similar analysis to that presented here. These authors also present detections of 850 μm emission from these clusters which, for Abell 1835, they suggest is likely to be due to dust heated by the vigorous star formation observed in the cluster core or an obscured active galactic nucleus.

Following Helou *et al.* (1988) and Wise *et al.* (1993), we can estimate the total infrared luminosities implied by the observed IRAS fluxes and flux limits using the relation

$$L_{1-1000\mu\text{m}} \sim 2.8 \times 10^{44} \left(\frac{z}{0.05}\right)^2 (2.58S_{60} + S_{100}) \text{ erg s}^{-1}, \quad (4)$$

where S_{60} and S_{100} are the 60 and 100 μm IRAS fluxes in units of Jy. This relation assumes a dust temperature of $\sim 30\text{K}$ (which is consistent with the observations; *e.g.* Allen *et al.* 1999; Edge *et al.* 1999) and an emissivity index, n , in the range 0 – 2, where the emissivity is proportional to the frequency, ν^n . Where measurements, rather than upper limits, were obtained, we associate a systematic uncertainty

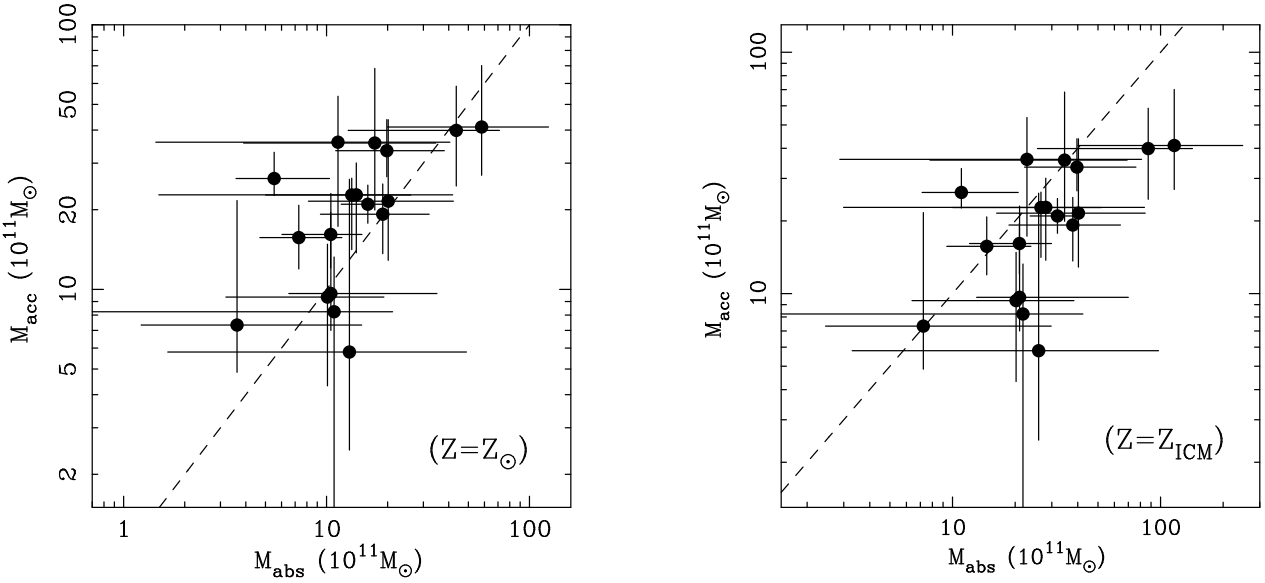


Figure 6. A comparison of the masses predicted to have been accumulated by the cooling flows within radii r_{abs} over the first 5 Gyr, versus the masses within the same radii implied by the observed intrinsic X-ray absorption (assuming the absorption to be due to cold gas with a covering fraction of unity). The dashed line indicates equality between the two sets of values. Results are shown both for (left) solar metallicity in the absorbing gas and (right) a metallicity of $0.4Z_{\odot}$.

of 30 per cent with the estimated $1 - 1000\mu\text{m}$ luminosities, which is combined in quadrature with the random errors. The $1 - 1000\mu\text{m}$ luminosities calculated from this relation are summarized in Table 11. In general, the measurements and upper limits to the observed $1 - 1000\mu\text{m}$ luminosities exceed the predicted luminosities due to reprocessed X-ray radiation from the cooling flows. Where measurements (rather than upper limits) are made, this may suggest the presence of an additional source of infrared flux, such as star formation or AGN associated with the central cluster galaxies, or some other contaminating (possibly Galactic) source. At some level, the massive starbursts at the centres of systems like Abell 1068, 1835, 2204 2390 and Zwicky 3146 (Allen 1995; Crawford *et al.* 1999; Edge *et al.* 1999) must contribute to the detected infrared flux.

6.4 Systematic uncertainties in the absorption measurements

As discussed in Section 6.1, the measured intrinsic equivalent hydrogen column densities of absorbing material inferred from the ASCA spectra exhibit significant systematic variation, depending upon whether the single-phase or multiphase emission models are used. We have adopted the results obtained with the cooling-flow model (model C) as our preferred values, since this model provides a consistent description of the spectral and imaging X-ray data for the clusters. However, a number of systematic uncertainties affecting the absorption results remain with the cooling flow model.

Spectral model C undoubtedly over-simplifies the situation in a real cooling flow. In particular, the model assumes that the absorbing material lies in a uniform screen in front

of the cooling flows. If the absorber is intrinsically associated with the clusters, then the absorbing material must, to some extent, be distributed throughout the cooling flows. Allen & Fabian (1997; see also Wise & Sarazin 1999) discuss two different, limiting geometries for the absorbing material; partial covering and multilayer absorption. The partial covering model, with a covering factor $f < 1$, can be expected to apply or where there are < 1 individual absorbing clouds along each line of sight and/or where the absorbing material is strongly clumped on large scales. However, as discussed in Section 6.1, covering fractions significantly less than unity are found to provide a poor description of the ASCA spectra, suggesting that the absorbing material is likely to be more smoothly distributed throughout the cooling flows.

The multilayer absorption model discussed by Allen & Fabian (1997) is applicable where the absorbing material is made up of a large number of similarly sized absorbing clouds, each with a column density much less than the total intrinsic column density (ΔN_{H}), homogeneously distributed throughout the X-ray emitting medium. For an intrinsic emission spectrum $A(E)$, the observed spectrum, $A'(E)$, emerging from the emitting/absorbing region may be written (where $\sigma(E)$ is the absorption cross-section) as

$$A'(E) = A(E) \left(\frac{1 - e^{-\sigma(E)\Delta N_{\text{H}}}}{\sigma(E)\Delta N_{\text{H}}} \right). \quad (5)$$

We have simulated cooling flow spectra with multilayer absorption, with total column densities of between 10^{21} and 5×10^{22} atom cm^{-2} , and fitted these with simple models which assume that the absorbing material acts as a uniform screen in front of the cooling flow (as with model C). For the simulations we adopt an emission spectrum appropriate for a constant pressure cooling flow, with an upper temperature of

7 keV and a metallicity of $0.4Z_{\odot}$. We use a response matrix appropriate for the ASCA SIS detectors. The comparison between the fitted (uniform screen) column densities and the true total (multilayer) values are shown in Fig. 7. We see that for multilayer column densities of $10^{21} - 5 \times 10^{22}$ atom cm^{-2} , the fitted column densities underestimate the true values by factors of 5–10. (These results are not sensitive to any reasonable choice of Galactic column density.)

If the multilayer model approximates the true distribution of X-ray emitting and absorbing material in cooling flows, then the results obtained with spectral model C would imply true equivalent column-densities of intrinsic absorbing gas in the cluster cores of, typically, a few 10^{22} atom cm^{-2} . Importantly, we also note that for signal-to-noise ratios appropriate for ASCA observations of bright clusters (with count rates of $\sim 1\text{ct s}^{-1}$ in the SIS detectors and exposure times of ~ 40 ks), the simple uniform-screen absorption model provides a good fit to the simulated spectra with multilayer absorption, for total column densities $\lesssim 3 \times 10^{22}$ atom cm^{-2} . (For larger total column densities, complex residuals are detected in the spectra at energies $\lesssim 2.0\text{keV}$.) The large intrinsic column densities implied by the multilayer models would have strong implications for the nature of the absorbing matter. In particular, column densities of $\gtrsim 10^{22}$ atom cm^{-2} of gaseous material with solar metallicity would be very difficult to reconcile with current HI and CO limits, even if this material were very cold and highly molecular. (We also note that in the case of a multilayer distribution, the implied masses of absorbing gas would often exceed the predicted accumulated masses due to the cooling flows and imply, at least in part, some other origin for the absorbing medium.) In the following section, we explore these issues in more detail and summarize the current observational constraints on the physical nature of the absorbing matter.

7 SEARCHES FOR THE X-RAY ABSORBING MATERIAL IN OTHER WAVEBANDS

The results presented in this paper provide a consistent picture for the X-ray properties of cooling flows in X-ray luminous clusters of galaxies. The ASCA spectra and ROSAT images provide independent determinations of the mass cooling rates in the clusters in good agreement with each other, when a consistent method of analysis is employed (Section 5.1). The spectral data require the presence of large column densities of intrinsic X-ray absorbing material associated with the cooling gas (Section 6). The implied masses of absorbing material are in reasonable agreement with the masses expected to have been accumulated by the cooling flows over their lifetimes (Section 6.2), identifying this material as a plausible sink for the bulk of the cooled gas from the flows. Despite the evidence for intrinsic X-ray absorption associated with cooling flows, however, searches for this material in other wavebands have, to date, proved largely unsuccessful (at least outside of the central 5–20 kpc). We here briefly review these observations and comment on their implications for the physical state of the X-ray absorbing matter. More detailed discussions of a number of these issues are given by Ferland, Fabian & Johnstone (1994), Daines, Fabian & Thomas (1994), Fabian *et al.* (1994a), O'Dea *et*

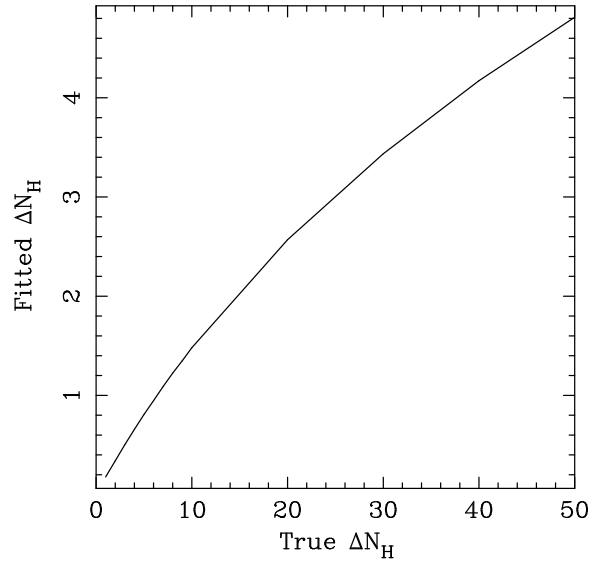


Figure 7. The apparent column density determined from fits to cooling flow spectra with a uniform-screen absorption model (*e.g.* spectral model C) when in reality the absorber is distributed in a multilayer manner (Allen & Fabian 1997). The vertical axis shows the fitted column density and the horizontal axis the true total (multilayer) column density through the emitting/absorbing region. Both axes are in units of 10^{21} atom cm^{-2} .

al. (1994a), Voit & Donahue (1995), O'Dea & Baum (1996), Arnaud & Mushotzky (1988) and Henkel & Wiklind (1998).

As mentioned in Section 5.2, the central (5–20 kpc) regions of CF clusters are commonly observed to be sites of ongoing star formation with powerful, associated optical line emission (*e.g.* Johnstone *et al.* 1987; Heckman *et al.* 1989; McNamara & O'Connell 1989; Crawford & Fabian 1992; Allen 1995; Cardiel *et al.* 1995, 1998; McNamara *et al.* 1996; Voit & Donahue 1997; Crawford *et al.* 1999). Nearly all CF clusters with short central cooling times ($t_{\text{cool}} \lesssim 2\text{Gyr}$) exhibit such phenomena (Peres *et al.* 1998), whereas systems with longer central cooling times (including all NCF clusters) generally do not. The observed levels of star formation imply the presence of at least moderate masses of cooled gas in the cores of CF clusters, sufficient in a few cases to account for the bulk of the mass deposited by the cooling flows in those regions (Allen 1995) and at least some causal connection with the cooling flows.

At radio wavelengths, extensive searches have been carried out for 21cm line-emission associated with warm atomic hydrogen in the cores of CF clusters (*e.g.* Valentijn & Giovanelli 1982; O'Dea & Baum 1996). The negative results obtained (with the exception of M87; Jaffe 1992) typically constrain the column densities of optically thin material to be less than a few 10^{19} atom cm^{-2} and, for an assumed spin temperature, $T_S \sim 20\text{K}$, the number of clouds along the line of sight to be $\lesssim 1$ (O'Dea & Baum 1996).

Searches have also been made for the 21 cm absorption signature of cold atomic hydrogen (*e.g.* McNamara, Bregman & O'Connell 1990; Jaffe 1992; Dwarakanath, van Gorkom & Owen 1994; O'Dea, Gallimore & Baum 1995;

O'Dea & Baum 1996; Johnstone *et al.* 1998). Such material has been detected across the central few kpc of a few CF clusters, including Abell 426 (Crane, Van der Hulst & Haschick 1982; Sijbring *et al.* 1989; Jaffe 1990) 2A0335+096 (McNamara *et al.* 1990), Hydra A (Dwarakanath, van Gorkom & Owen 1995), MKW3s (McNamara *et al.* 1990) and Abell 2597 (O'Dea, Baum & Gallimore 1994) with typical column densities of a few $10^{20} (T_{\text{S}}/100)$ atom cm $^{-2}$. However, for most clusters only negative results have been obtained, with upper limits to the column densities of 10K gas (assuming a covering fraction of unity and a velocity width of ~ 1.5 kms $^{-1}$; Dwarakanath *et al.* 1994, O'Dea & Baum 1996) of $10^{18} - 10^{19}$ atom cm $^{-2}$.

Laor (1997) presents tight limits on the column density of atomic hydrogen towards the core of Abell 426 ($\Delta N_{\text{H}} \lesssim 4 \times 10^{17}$ atom cm $^{-2}$) from Ly α observations made with the Hubble Space Telescope (see also Johnstone & Fabian 1995). Together, the results on HI emission and absorption, and Ly α absorption, imply that the bulk of the material responsible for the observed X-ray absorption cannot be in the form of atomic hydrogen.

An issue of crucial importance in interpreting the 21cm HI results and the results from CO studies (see below) is the expected temperature of X-ray absorber, if in gaseous form, which has proved controversial. Johnstone, Fabian & Taylor (1998; updating earlier calculations by Ferland, Fabian & Johnstone 1994 and Fabian *et al.* 1994a) suggest that cooled gas clouds, in equilibrium with the cooling-flow environment, are likely to be very cold. Johnstone *et al.* (1998) suggest that dust-free clouds form an extended outer envelope, with a column density of $\sim 5 \times 10^{21}$ atom cm $^{-2}$ and a temperature of 13-17K, beyond which the gas drops to the microwave background temperature. For Galactic dust/gas ratios, however, the results are significantly modified, such that the cloud temperature drops to the microwave background temperature after a column density of only $\sim 10^{20}$ atom cm $^{-2}$. At such low temperatures, dusty gas is likely to be highly molecular. However, these predictions differ from those of O'Dea *et al.* (1994a) and Voit & Donahue (1995) who suggest a minimum temperature for such clouds of ~ 20 K, even in the presence of dust. Braine *et al.* (1995) also suggest a minimum temperature of ~ 10 K for the absorbing gas. Possible reasons for the discrepancies between these results (with contrasting views) are discussed by Voit & Donahue (1995) and Ferland *et al.* (in preparation).

Extensive searches have been carried out for CO associated with molecular gas in cooling flows. To date CO emission has only been detected in Abell 426 (Lazareff *et al.* 1989; Mirabel, Sanders D.B. & Kazés I. 1989). Braine *et al.* (1995) also present limits on CO absorption in the central regions of this cluster). The upper limits to the column density of molecular hydrogen in the inner regions of other clusters (for an assumed kinetic temperature of $T_{\text{CO}}^{\text{K}} = 20$ K and a covering fraction of unity) are typically \lesssim a few 10^{20} atom cm $^{-2}$ (O'Dea *et al.* 1994a, Antonucci & Barvainis 1994, McNamara & Jaffe 1994; Braine & Dupraz 1995; O'Dea & Baum 1996) which is significantly below the X-ray inferred column densities. The CO results also constrain the number of clouds along the line of sight (for $T_{\text{CO}}^{\text{K}} = 20$ K) to be $\lesssim 10$ (O'Dea *et al.* 1994a; O'Dea & Baum 1996). The CO emission limits appear to exclude the possibility of large column densities (*i.e.* values consistent with the X-ray measurements)

of molecular gas, with a kinetic temperature $\gtrsim 10$ K. However, if the bulk of the X-ray gas cools to the microwave background temperature, as suggested by Johnstone *et al.* (1998), the CO limits may be consistent with the X-ray data.

It should be noted that the determinations of molecular hydrogen masses from CO observations are affected by a number of additional uncertainties. Firstly, the CO/H₂ ratios in cluster cooling flows may differ from Galactic values. In particular, where the temperature and metallicity of the absorbing gas is low, the use of a standard Galactic CO/H₂ ratio may underestimate the mass of molecular gas (Maloney & Black 1988; Madden *et al.* 1997).

It is unclear whether X-ray absorbing gas accumulated by cooling flows could have substantially sub-solar metallicity. Allen & Fabian (1998b) determine a mean emission-weighted metallicity for the X-ray emitting gas in CF clusters of $Z \sim 0.4Z_{\odot}$. These authors also show that CF clusters generally contain metallicity gradients, so that the metallicity of the X-ray gas within the cooling radii of CF systems will, on average, exceed this value. Thus, it seems unlikely that the material currently being deposited from the cooling flows will have substantially sub-solar metallicities. However, if the X-ray absorbing material is formed from the matter deposited by the cooling flows over their lifetimes, the metallicity of this material could be somewhat lower. Within an inhomogeneous cooling flow (*e.g.* Nulsen 1986, 1998; Thomas, Fabian & Nulsen 1987) the denser gas at any particular radius will tend to have a smaller volume filling factor. If the metals are evenly distributed throughout the volume of the cooling flow at any particular radius (whether this will occur is unclear), the least dense gas will contain most of the metals (Reisenegger, Miralda-Escudé & Waxman 1996). Since the densest material in cooling flows will have the shortest cooling time and be deposited first, the material accumulated by the cooling flows over their histories could have a significantly lower metallicity than the material being deposited today. Conversely, if the metals in cooling flows were concentrated in the densest material, the metallicity of the X-ray absorbing material could exceed that of the X-ray emitting gas.

Fabian *et al.* (1994a), have suggested that the masses of molecular gas inferred from CO observations could be significantly underestimated if most of the CO in the absorbing material has frozen onto dust grains. Such freezing should occur rapidly (on timescales $\sim 10^5$ yr) if even small amounts of dust are initially present in the absorbing gas (Voit & Donahue 1995). Daines *et al.* (1994) and Fabian *et al.* (1994a) discuss how dust is likely to form even in clouds that are initially free of dust, on timescales $\sim 10^9$ yr (although see also Voit & Donahue 1995). Optical, UV and sub-mm studies of the cores of cooling flows show that dust lanes (*e.g.* Sparks, Macchetto & Golombek 1989; McNamara & O'Connell 1992) and intrinsic reddening (Hu 1992; Allen *et al.* 1995; Edge *et al.* 1999) are common.

Elston & Maloney (1994) and Jaffe & Bremer (1997) report detections of H₂(1-0)S(1) emission from warm (~ 2000 K) molecular hydrogen from K-band spectroscopy of the inner few kpc of a number of CF systems (including Abell 478 and PKS0745-191). No detections of such emission have been made in NCF systems. The H₂S emission is likely to arise from the heated skin of cold molecular clouds

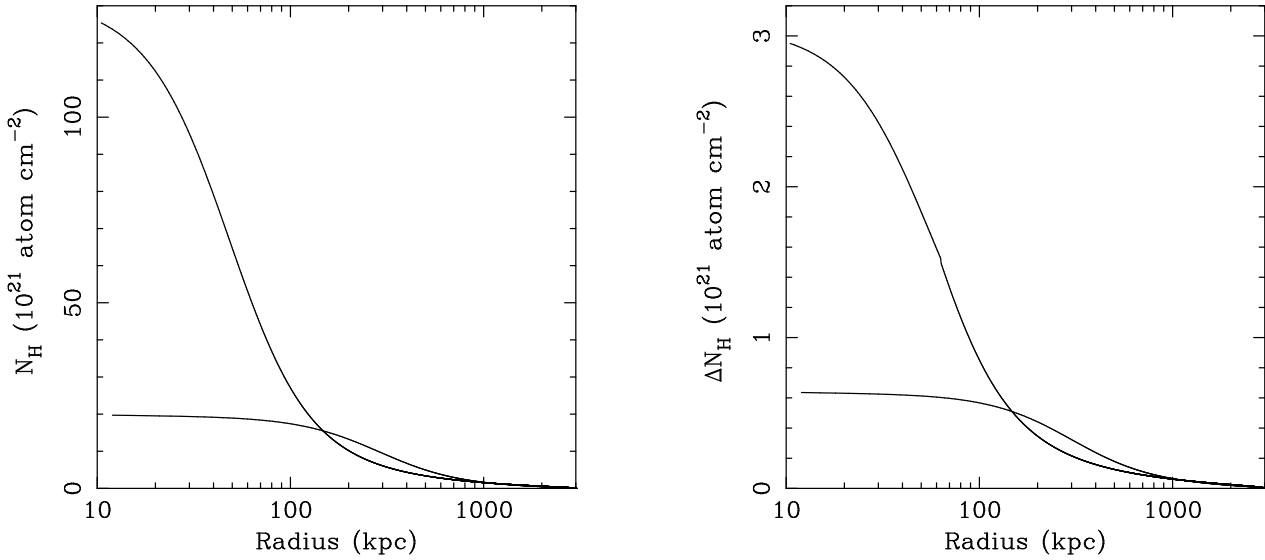


Figure 8. (a) The equivalent column densities of hot hydrogen ions through two simulated clusters, one CF and one NCF system. The gas distributions have been modeled as isothermal spheres, with core radii of 50 kpc (CF; upper curve) and 300 kpc (NCF; lower curve) respectively, and have been normalized to provide total X-ray gas masses within radii of 3Mpc of $2 \times 10^{14} M_{\odot}$. The distribution of X-ray emitting gas is much more centrally concentrated in the CF cluster, particularly within the central 100 – 200 kpc. (b) The X-ray absorbing column density, as a function of radius, due to dust distributed throughout the simulated CF (upper curve) and NCF (lower curve) clusters. The dust is assumed to have a multilayer distribution within the X-ray emitting gas, but be modeled as a simple uniform screen in front of the clusters.

which could also be responsible for the optical emission-line phenomena discussed above.

A final possibility, first discussed in detail by Voit & Donahue (1995; see also Arnaud & Mushotzky 1998), is that the X-ray absorption could be due to dust, with little or no associated gas. The K-absorption edge of oxygen is a primary source of X-ray absorption and its signature is fairly insensitive to the physical state of the oxygen, so long as it is not highly ionized. The introduction of a simple OIK absorption edge at $E \sim 0.54$ keV in the ASCA analysis (such as might be associated with oxygen-rich, silicate dust grains) typically provides at least as good a model for the intrinsic absorption as a cold gaseous absorber. Arnaud & Mushotzky (1998) have shown that 0.35 – 7.0 keV Broad Band X-ray Telescope data for the Perseus cluster require excess absorption which is significantly better-explained by a simple oxygen absorption edge (which they associate with dust) than by a cold, gaseous absorption model. Verification of this important result will be possible in the near future using observations made with the Chandra Observatory and XMM.

Optical and UV spectroscopy of the central emission-line nebulosities in cooling flows indicate the presence of significant amounts of dust (Hu 1992; Allen *et al.* 1995; Crawford *et al.* 1999). Allen *et al.* (1995) also show that the column densities of absorbing gas inferred from the optical reddening studies are in reasonable agreement with the X-ray values, for Galactic dust/gas ratios. The infrared observations reported here and elsewhere, together with the sub-mm results of Edge *et al.* (1999), require the presence of significant dust masses in the core regions of at least a

few nearby and/or exceptionally massive cooling flows (for which the best data exist) and are consistent with dust being a common feature of CF clusters. Limits on background counts of galaxies and quasars behind clusters are consistent with extinctions ranging from $A_B = 0.2 - 0.5$ (e.g. Boyle, Fong & Shanks 1988; Romani & Maoz 1992), although measurements of galaxy colours in nearby clusters constrain the reddening on cluster-wide scales to be $E(B - V) < 0.06$ mag (Ferguson 1993).

Voit & Donahue (1995) argue that the levels of dust required to account for the observed X-ray absorption are unlikely to lie entirely within the cores of the clusters, and should be distributed more widely throughout the cluster gas. ROSAT results on the spatial distribution of the X-ray absorbing material (Allen & Fabian 1997) show it to be centrally concentrated within the cooling radii of clusters and possibly be confined within cooling flows. However, the X-ray data are also consistent with a scenario in which the absorbing material is distributed in a manner similar to the X-ray emitting gas. This is illustrated in Fig. 8(a), where we show the equivalent column densities of hydrogen ions in the X-ray emitting gas through two simulated clusters; one CF and one NCF system. The gas distributions have been modeled as isothermal spheres, with core radii of 50 and 300 kpc, respectively (and have been normalized to provide total X-ray gas masses within 3Mpc of the cluster centres of $2 \times 10^{14} M_{\odot}$). We see that the distribution of X-ray emitting gas is much more centrally concentrated in the CF system, particularly within the central ~ 100 kpc.

Fig. 8(b) shows the corresponding X-ray absorbing column densities as a function of radius (as would be deter-

mined from observations with ASCA-like CCD detectors in the 0.6 – 10.0 keV band) in the case where the intracluster gas has an equivalent metallicity in dust grains of ~ 0.2 solar. For simplicity, we assume that the dust has an absorption spectrum in the ASCA band similar to that of metal-rich cold gas (Morrison & McCammon 1983; qualitatively similar results are obtained for an oxygen edge at 0.54 keV). We also assume that the absorber follows a multilayer distribution within the X-ray emitting medium, but is modeled as a uniform absorbing screen in front of the emitting regions. The results imply mean emission-weighted column densities (where we assume the X-ray emissivity to be proportional to square of the gas density) of $\sim 2 \times 10^{21}$ atom cm^{-2} for the CF cluster, and a few $\times 10^{20}$ atom cm^{-2} for the NCF system. (The absolute results on the excess column densities will depend upon the chemical composition of the dust). We thus see that if the X-ray absorption is due to dust, with a spatial distribution that follows the X-ray gas, then we can expect absorption signatures to be present in both CF and NCF clusters, but to be stronger in CF systems (assuming in each case that an appropriate spectral model is used in the analysis). We would also expect the absorption to be concentrated towards the cores of CF clusters, in agreement with the observations. We note that if the X-ray absorption were entirely due to a pre-existing distribution of dust grains distributed throughout the clusters, then the agreement between the observed masses of absorbing matter (calculated assuming that the absorption is due to cold gas confined within the cooling flows) and the masses predicted to have been accumulated by the cooling flows over their lifetimes (Fig. 6) must be regarded as coincidence. However, it remains possible that both material accumulated by the cooling flows and a more extended distribution of large dust grains (presumably due to supernovae enrichment at early epochs) could contribute to the X-ray absorption.

The lifetime of grains of radius $a\mu\text{m}$ to sputtering in hot gas of density n is $\sim 2 \times 10^6 a/n \text{ yr}$ (Draine & Salpeter 1979). Provided that individual grains exceed $10\mu\text{m}$ in radius, they should survive for a Hubble time or longer throughout NCF clusters and beyond the cooling radius in clusters with cooling flows. Within cooling flows, the gas density rises inward so the grains are increasingly sputtered, releasing the metals into the gas phase which thus becomes increasingly metal rich towards the cluster centre. This provides one possible explanation for the abundance gradients inferred to be present in most CF clusters (Allen & Fabian 1998b; see also Irwin & Bregman 1999). However, $10\mu\text{m}$ grains are optically thick to soft X-rays and so some distribution of grain sizes extending to smaller values is required if dust is responsible for the observed X-ray absorption (*e.g.* Laor & Draine 1993). We note that the sputtering of small ($a \lesssim 0.1\mu\text{m}$) grains will significantly modify the reddening law in clusters with respect to the standard Galactic relation, reducing the optical/UV reddening (Laor & Draine 1993).

In conclusion, the available data from other wavebands provide some support for the large column densities of intrinsic absorbing material inferred to be present from the X-ray data, at least in the innermost regions of cooling flows. Optical and sub-mm observations of star formation in the cores of CF clusters and K-band observations of emission lines from molecular hydrogen suggest that significant masses of dusty, molecular gas are present in the central few tens of kpc of

many CF clusters. The constraints from 21cm observations suggest that the bulk of the material accumulated by cooling flows cannot remain in a long-lived reservoir of atomic hydrogen. Substantial masses of molecular gas may be distributed throughout cooling flows and as yet have avoided detection, but this material must be very cold ($T \sim 3\text{K}$) and dusty, a possibility that remains controversial. The very large X-ray column densities ($\gtrsim 10^{22}$ atom cm^{-2}) required if the absorbing material has a multilayer distribution are probably incompatible with a gaseous absorber. It remains possible that dust grains, either present in the cooled material deposited by the cooling flows or distributed throughout the clusters in a manner similar to the X-ray gas, may be responsible for much of the observed X-ray absorption.

8 CONCLUSIONS

The main conclusions that may be drawn from this paper may be summarized as follows:

(i) We have demonstrated the need for multiphase models to consistently explain the spectral and imaging X-ray data for the CF clusters included in our study. The mass deposition rates from the cooling flows, independently inferred from multiphase analyses of the ASCA spectra and deprojection analyses of the ROSAT HRI images, exhibit good agreement, especially once the effects of intrinsic X-ray absorption have been accounted for in a consistent manner. The mass deposition rates from the largest cooling flows exceed $1000 \text{ M}_\odot \text{ yr}^{-1}$, identifying these as some of the most massive cooling flows known.

(ii) We have confirmed the presence of intrinsic X-ray absorption in the cluster spectra using a variety of spectral models. The measured equivalent hydrogen column densities are sensitive to the spectral models used in the analysis, ranging from a few 10^{20} atom cm^{-2} for a simple isothermal emission model to a few 10^{21} atom cm^{-2} using our preferred cooling-flow models, assuming in each case that the absorber lies in a uniform foreground screen. Both the CF and NCF systems exhibit excess absorption at a similar level (on average) when analysed with the same, simple isothermal model.

(iii) The masses of X-ray absorbing material inferred to be present in the CF clusters (assuming the absorption to be due to cold gas with a covering fraction of unity) are in reasonable agreement with the masses expected to have been accumulated by the cooling flows over their lifetimes.

(iv) The ASCA spectra constrain the covering fraction of the absorbing material acting on the cooling flows to be close to (or exceed) unity. If the X-ray absorption is due to many small, similarly-sized clouds along each line of sight, intermixed with the X-ray emitting gas, then the column densities inferred from the spectral analysis may significantly underestimate the true column densities of absorbing material in the cooling flows.

(vii) We have summarized the constraints on the physical properties of the X-ray absorbing material from observations in other wavebands. Substantial 60 and $100\mu\text{m}$ fluxes, sufficient to account for the bolometric luminosities absorbed and reprocessed within the clusters, are detected from several of the largest cooling flows. Optical observations of star formation in the cores of cooling flows also suggests that significant masses of molecular gas are present

in the central few tens of kpc of many CF systems. Constraints from 21cm observations suggest that the bulk of the material accumulated within the cooling radii cannot remain in a long-lived reservoir of atomic hydrogen. Substantial masses of molecular gas may be distributed throughout cooling flows and as yet have avoided detection, although this material must be very cold ($T \sim 3K$), a possibility that remains controversial. The very large X-ray column densities ($\gtrsim 10^{22} \text{ atom cm}^{-2}$) required if the absorbing material has a multilayer distribution are probably incompatible with a gaseous absorber. It remains possible that dust grains, either present in the material accumulated by the cooling flows or distributed more widely in a manner similar to the X-ray gas, may be responsible for much of the X-ray absorption.

ACKNOWLEDGMENTS

I thank Andy Fabian, Roderick Johnstone and Dave White for many helpful discussions and Harald Ebeling, Alastair Edge and Carolin Crawford for their continuing efforts with the BCS project. I acknowledge the support of the Royal Society.

REFERENCES

Allen S.W., 1995, MNRAS, 276, 947
 Allen S.W., 1998, MNRAS, 296, 392
 Allen S.W., Fabian A.C., 1997, MNRAS, 286, 583
 Allen S.W., Fabian A.C., 1998a, MNRAS, 297, L57
 Allen S.W., Fabian A.C., 1998b, MNRAS, 297, L63
 Allen S.W., Fabian A.C., Johnstone R.M., White D.A., Daines S.J., Edge A.C., Stewart G.C., 1993, MNRAS, 262, 901
 Allen S.W., Fabian A.C., Edge A.C., Böhringer H., White D.A., 1995, MNRAS, 275, 741
 Allen S.W., Fabian A.C., Edge A.C., Bautz M.W., Furuzawa A., Tawara Y., 1996, MNRAS, 283, 263
 Allen S.W., Fabian A.C., Johnstone R.M., Arnaud K.A., Nulsen P.E.J., 1999, MNRAS, submitted
 Akritas M.G., Bershadsky M.A., 1996, ApJ, 470, 706
 Anders E., Grevesse N., 1989, Geochimica et Cosmochimica Acta 53, 197
 Antonucci R., Barvainis R., 1994, AJ, 107, 448
 Arnaud, K.A., 1996, in Astronomical Data Analysis Software and Systems V, eds. Jacoby G. and Barnes J., ASP Conf. Series volume 101, p17
 Arnaud K.A., 1988, in Fabian A.C., ed, Cooling Flows in Clusters and Galaxies. Kluwer, Dordrecht, p. 31
 Arnaud K.A., Mushotzky R.F., 1998, ApJ, 501, 119
 Balucinska-Church M., McCammon D., 1992, ApJ, 400, 699
 Bevington P.R., 1969, Data reduction and Error analysis for the Physical Sciences. McGraw-Hill, New York
 Binney J., Tremaine S., 1987, Galactic Dynamics, Princeton Univ. Press, Princeton
 Böhringer H., Tanaka Y., Mushotzky R.F., Ikebe Y., Hattori M., 1998, A&A, 334, 789
 Boyle B.J., Fong R., Shanks T., 1988, MNRAS, 231, 897
 Braine J., Dupraz C., 1994, A&A, 283, 407
 Braine J., Wyrowski F., Radford S.J.E., Henkel C., Lesch H., 1995, A&A, 293, 315
 Buote D.A., Tsai J.C., 1996, ApJ, 458, 27
 Cardiel N., Gorgas J., Aragon-Salamanca A., 1995, MNRAS, 277, 502
 Cardiel N., Gorgas J., Aragon-Salamanca A., 1998, MNRAS, 298, 977
 Cavaliere A., Fusco-Femiano R., 1976, A&A, 49, 137
 Cavaliere A., Fusco-Femiano R., 1978, A&A, 49, 137
 Cox C.V., Bregman J.N., Schombert J.M., 1995, ApJS, 99, 405
 Crane P., Van der Hulst J.M., Haschick A., 1982, IAUS, 97, 307
 Crawford C.S., Fabian A.C., 1992, MNRAS, 259, 265
 Crawford C.S., Allen S.W., Ebeling H., Edge A.C., Fabian A.C., 1999, MNRAS, 306, 857
 Daines S.J., Fabian A.C., Thomas, P.A., 1994, MNRAS, 268, 1060
 David L.P., Slyz A., Jones C., Forman W., Vrtilek S.D., Arnaud K.A., 1993, ApJ, 412, 479
 David L.P., Harnden F.R., Kearns K.E., Zombeck M.V., 1996, The ROSAT HRI Calibration Report, [ftp://legacy.gsfc.nasa.gov/rosat/doc/hri/hri_report](http://legacy.gsfc.nasa.gov/rosat/doc/hri/hri_report)
 Dickey J.M., Lockman F.J., 1990, ARA&A, 28, 215
 Draine B.T., Salpeter E.E., 1979, ApJ, 231, 77
 Dwarakanath K.S., van Gorkom J.H., Owen F.N., 1994, ApJ, 432, 469
 Dwarakanath K.S., Owen F.N., van Gorkom J.H., 1995, ApJ, 442, L1
 Dwek E., Rephaeli Y., Mather J.C., 1990, ApJ, 350, 104
 Ebeling H., Voges W., Böhringer H., Edge A.C., Huchra J.P., Briel U.G., 1996, MNRAS, 281, 799
 Ebeling H., Edge A.C., Böhringer H., Allen S.W., Crawford C.S., Fabian A.C., Voges W., Huchra J.P., 1998, MNRAS, 301, 881
 Edge A.C., Stewart G.C., Fabian A.C., 1992, MNRAS, 258, 177
 Edge A.C., Ivison RR.J., Smail I., Blain A.W., Kneib J.-P., 1999, MNRAS, 306, 599
 Elston R., Maloney P., 1994, in Infrared Astronomy with Arrays, ASSL, 190, Kluwer, Dordrecht, p. 169
 Fabian A.C., 1994, A&AR, 32, 277
 Fabian A.C., Nulsen P.E.J., Canizares C.R., 1991, A&AR, 2, 191
 Fabian A.C., Johnstone R.M., Daines S.J., 1994a, MNRAS, 271, 737
 Fabian A.C., Hu E.M., Cowie L.L., Grindlay J., 1981, ApJ, 248, 47
 Fabian A.C., Arnaud K.A., Bautz M.W., Tawara Y., 1994b, ApJ, 436, L63
 Ferguson H.C., 1993, MNRAS, 263, 343
 Feretti L., Giovannini G., Böhringer H., 1997, NewA, 2, 501
 Ferland G.J., Fabian A.C., Johnstone R.M., 1994, MNRAS, 266, 399
 Fukazawa Y. et al. 1994, PASJ, 46, L55
 Heckman T.M., Baum S.A., Van Breugel W.J.M., McCarthy P., 1989, ApJ, 338, 48
 Helou G., Khan I.R., Malek L., Boehmer L., 1988, ApJS, 68, 151
 Henkel C., Wiklind T., 1997, SSRv, 81, 1
 Hu E.M., 1992, ApJ, 391, 608
 Ikebe Y., Makishima K., Fukazawa Y., Tamura T., Xu H., Ohashi T., Matsushita K., 1999, ApJ, in press
 Irwin J.A., Bregman J.N., 1999, ApJ, submitted
 Irwin J.A., Sarazin C.L., 1995, ApJ, 355, 497
 Jaffe W., 1990, A&A, 240, 254
 Jaffe W., 1992, in Fabian A.C., ed., Clusters and Superclusters of Galaxies, Kluwer, Dordrecht, p. 109
 Jaffe W., Bremer M.N., 1997, MNRAS, 284L, 1
 Johnstone R.M., Fabian A.C., 1995, MNRAS, 273, 625
 Johnstone R.M., Fabian A.C., Nulsen P.E.J., 1987, MNRAS, 224, 75
 Johnstone R.M., Fabian A.C., Taylor G.B., 1998, MNRAS, 298, 854
 Johnstone R.M., Fabian A.C., Edge A.C., Thomas P.A., 1992, MNRAS, 255, 431
 Jones C., Forman W., 1984, ApJ, 276, 38
 Kaastra J.S., Mewe R., 1993, Legacy, 3, HEASARC, NASA
 Kleinmann S.G., Hamilton D., Keel W.C., Wynn-Williams C.G., Eales S.A., Becklin E.E., Kuntz K.D., 1988, ApJ, 328, 161
 Kneib J.-P., Mellier Y., Pelló R., Miralda-Escudé J., Le Borgne J.-F., Böhringer H., Picat J.-P., 1995, A&A, 303, 27

Laor A., 1997, *ApJ*, 483, L103
 Laor A., Draine B.T., 1993, *ApJ*, 402, 441
 Lazareff B., Castets A., Kim D.-W., Jura M., 1989, *ApJ*, 336, L13
 Liedahl D.A., Osterheld A.L., Goldstein W.H., 1995, *ApJ*, 438, L115
 Madden S.C., Poglitsch A., Geis N., Stacey G.J., Townes C.H., 1997, 483, 200
 Maloney P., Black J.H., 1988, *ApJ*, 325, 389
 Makishima K., 1997, in Makino F., Mitsuda K., eds., X-ray Imaging and Spectroscopy of Cosmic Hot Plasmas, Universal Academy Press, Tokyo, p. 137
 Markevitch M., 1996, *ApJ*, 465, L1
 Markevitch M., Forman W.R., Sarazin C.L., Vikhlinin A., 1998, *ApJ*, 503, 77
 Matsumoto H., Koyama K., Awaki H., Tomida H., Tsuru T., Mushotzky R., Hatsukade I., 1996, *PASJ*, 48, 201
 McNamara B.R., Jaffe W., 1994, *A&A*, 281, 673
 McNamara B.R., O'Connell R.W., 1989, *AJ*, 98, 2018
 McNamara B.R., O'Connell R.W., 1992, *ApJ*, 393, 589
 McNamara B.R., Bregman J.N., O'Connell, 1990, *ApJ*, 360, 20
 McNamara B.R., Jannuzi B.T., Elston R., Sarazin C.L., Wise M., 1996, *ApJ*, 469, 66
 Mirabel I.F., Sanders D.B., Kazés I., 1989, *ApJ*, 340, L9
 Morrison R., McCammon D., 1983, *ApJ*, 270, 119
 Moshir M. *et al.*, 1989. Explanatory Supplement to the IRAS Faint Source Survey. IPAC preprint 44
 Nulsen P.E.J., 1986, *MNRAS*, 221, 377
 Nulsen P.E.J., 1998, *MNRAS*, 297, 1109
 O'Dea C.P., Baum S.A., 1996, in Cold gas at high redshift, eds. Bremer M.N., van der Werf P.P., Röttgering H.J.A., Carilli C.L., Kluwer, Dordrecht, p.199
 O'Dea C.P., Baum S.A., Gallimore J.F., 1994b, *ApJ*, 436, 669
 O'Dea C.P., Gallimore J.F., Baum S.A., 1995, *AJ*, 109, 26
 O'Dea C.P., Baum S.A., Maloney P.R., Tacconi L.J., Sparks W.B., 1994a, *ApJ*, 422, 467
 Peres C.B., Fabian A.C., Edge A.C., Allen S.W., Johnstone R.M., White D.A., 1998, *MNRAS*, 298, 416
 Press W.H., Teukolsky S.A., Vetterling W.T., Flannery B.P., 1992, Numerical Recipes, Cambridge University Press
 Reisenegger A., Miralda-Escudé J., Waxman E., 1996, *ApJ*, 457, 11L
 Rizza E., Burns J.O., Ledlow M.J., Owen F.N., Voges W., Bliton M., 1998, *MNRAS*, 301, 328
 Romani R.W., Maoz D., 1992, *ApJ*, 386, 36
 Schindler S., Hattori M., Neumann D.M., Böhringer H., 1997, *A&A*, 317, 646
 Sijbring D., De Bruyn A.G., Jaffe W.J., Sancisi R., in Meurs E.J.A., Fosbury R.A.E., eds., Extranuclear Activity in Galaxies, European Southern Observatory, 1989, Garching bei München, p107
 Smail I., Hogg D.W., Blandford R., Cohen J.G., Edge A.C., Djorgovski S.G., 1995, *MNRAS*, 277, 1
 Smail I., Ellis R.E., Dressler A., Couch W.J., Oemler A., Sharples R.M., Butcher H., 1997, *ApJ*, 479, 70
 Sparks W.B., Macchetto F., Golombek D., 1989, *ApJ*, 345, 153
 Squires G., Neumann D.M., Kaiser N., Arnaud M., Babul A., Böhringer H., Fahlman G., Woods D., 1997, *ApJ*, 482, 648
 Tanaka Y., Inoue H., Holt S.S., 1994, *PASJ*, 46, L37
 Thomas P.A., Fabian A.C., Nulsen P.E.J., 1987, *MNRAS*, 228, 973
 Valentijn E.A., Giovanelli R., 1982, *A&A*, 114, 208
 Voit G.M., Donahue M., 1995, *ApJ*, 452, 164
 Voit G.M., Donahue M., 1997, *ApJ*, 486, 242
 Waxman E., Miralda-Escudé J., 1995, *ApJ*, 451, 451
 White D.A., Fabian A.C., Johnstone R.M., Mushotzky R.F., Arnaud K.A., 1991, *MNRAS*, 252, 72
 White D.A., Jones C., Forman W., 1997, *MNRAS*, 292, 419
 Wise M.W., Sarazin C.L., 1999, *ApJ*, submitted
 Wise M.W., O'Connell R.W., Bregman J.N., Roberts M.S., 1993, *ApJ*, 405, 94

Table 1. Summary of the ASCA Observations

Cluster	z	N_{H}	Date	S0	S1	G2	G3
Abell 2744	0.308	0.16	1994 Jul 04	37605	26086	62749	62753
Abell 478 [†]	0.088	3.00	1994 Feb 24	27953	—	34560	34554
Abell 520	0.203	0.78	1994 Sep 09	16802	15871	17656	17617
Abell 586	0.171	0.52	1994 Mar 22	8482	—	17668	17648
PKS0745-191	0.103	4.24	1993 Nov 06	29146	—	37553	37553
Abell 665	0.182	0.42	1993 Sep 18	22926	19869	34815	34799
IRAS 09104+4109	0.442	0.10	1993 Nov 12	33447	24348	38655	38655
Abell 773	0.217	0.14	1994 Nov 22	38500	38086	40841	40831
Abell 963	0.206	0.14	1993 Apr 22	29611	29039	29883	29881
Zwicky 3146	0.291	0.30	1993 May 18	29663	28643	32622	32632
Abell 1068	0.139	0.14	1996 Dec 06	23777	23645	21463	21639
Abell 1413	0.143	0.22	1993 Dec 11	26084	19862	36173	36175
Abell 1689	0.184	0.18	1993 Jun 26	29575	23642	37817	37817
Abell 1704	0.216	0.18	1994 Apr 16	18847	11784	20598	20596
RXJ1347.5-1145	0.451	0.49	1995 Jan 17	27882	17549	38968	38958
Abell 1795	0.063	0.12	1993 Jun 16	31284	—	37649	37641
MS1358.4+6245	0.327	0.19	1995 Apr 27	32532	30815	31981	31513
Abell 1835 #1	0.252	0.23	1994 Jul 20	18051	17532	17464	17460
Abell 1835 #2	”	”	1994 Jul 21	16876	16444	16412	16410
MS1455.0+2232	0.258	0.32	1994 Jul 18	29388	28539	28903	28895
Abell 2029	0.077	0.31	1994 Feb 19	34211	32420	35038	34963
Abell 2142	0.089	0.42	1994 Feb 21	12335	—	15768	15766
Abell 2163	0.208	1.21	1993 Aug 08	25126	18224	32760	32322
Abell 2204	0.152	0.57	1994 Aug 20	12749	11865	14698	14698
Abell 2218	0.175	0.32	1993 Apr 30	28241	26054	37970	37968
Abell 2219	0.228	0.18	1994 Aug 07	32705	31697	35849	35849
Abell 2261	0.224	0.33	1996 Feb 24	19224	18823	19249	19219
Abell 2319	0.056	0.80	1993 Jul 21	9842	5007	13169	13404
MS2137.3-2353	0.313	0.36	1994 May 08	15167	15732	17035	17056
Abell 2390	0.233	0.68	1994 Nov 13	6172	2632	10340	10338
AC114	0.312	0.13	1995 Nov 09	36739	36295	35987	35971

Notes: Columns 2 and 3 list the redshift and Galactic column density, in units of 10^{21} atom cm $^{-2}$ from Dickey & Lockman (1990), with the exception of Abell 478[†], for which the value is from Allen & Fabian (1997). For PKS0745-191, this study (Section 3.2) suggests a Galactic column density of $\sim 3.5 \times 10^{21}$ atom cm $^{-2}$, which is lower than the Dickey & Lockman (1990) value. Column 4 lists the dates of the ASCA observation. Columns 5 – 8 list the net exposure times (in seconds) in each of the four ASCA detectors, after all screening and cleaning procedures were carried out.

Table 2. Extraction radii for the ASCA spectra

Cluster	S0 (amin/kpc)	S1 (amin/kpc)	Chip mode
Abell 2744	3.4/1140	2.7/905	4(1)
Abell 478	3.8/503	—	4(1)
Abell 520	3.6/922	3.1/794	2(2)
Abell 586	3.6/814	—	4(1)
PKS0745-191	4.2/636	—	4(1)
Abell 665	4.5/1070	5.3/1260	4(2)
IRAS 09104+4109	4.0/1620	4.0/1620	4(4)
Abell 773	4.4/1180	3.9/1050	1
Abell 963	3.6/932	2.8/725	2(1)
Zwicky 3146	5.3/1720	4.3/1390	2(2)
Abell 1068	3.4/656	2.6/502	1
Abell 1413	4.0/790	4.0/790	4(4)
Abell 1689	4.0/955	4.0/955	4(4)
Abell 1704	3.4/909	2.6/695	4(1)
RXJ1347.5-1145	4.0/1630	4.0/1630	4(1)
Abell 1795	4.5/445	—	4(2)
MS1358.4+6245	3.9/1350	2.9/1010	4(2)
Abell 1835 #1	4.1/1220	3.2/948	2(1)
Abell 1835 #2	4.1/1220	3.2/948	2(1)
MS1455.0+2232	3.7/1110	2.8/842	2(1)
Abell 2029	3.5/413	2.7/319	2(1)
Abell 2142	6.0/802	—	4(4)
Abell 2163	3.7/964	4.5/1170	4(2)
Abell 2204	4.9/1010	4.7/973	2(1)
Abell 2218	3.7/852	2.5/575	4(1)
Abell 2219	5.3/1470	4.5/1250	2(1)
Abell 2261	4.5/1230	3.6/987	2(2)
Abell 2319	4.2/373	4.0/355	4(1)
MS2137.3-2353	4.3/1460	3.4/1150	2(2)
Abell 2390	3.6/1010	2.5/704	4(1)
AC114	3.4/1150	2.9/980	1

The radii of the circular extraction regions for the ASCA SIS data (in arcmin and kpc) and the chip modes used in the observations (either 1,2 or 4-CCD mode). The numbers in parentheses indicate the number of chips contributing to the extracted spectra. For the GIS data a fixed extraction radius of 6 arcmin was used. For Abell 2142, the 2 arcmin (3 arcmin) radius region surrounding the X-ray bright Seyfert-1 galaxy 1556+274 was masked out and excluded from the analysis for the SIS (GIS) data.

Table 3. Summary of the ROSAT Observations

Cluster	Date	Exposure (s)	R.A. (J2000.)	Dec. (J2000.)
Abell 2744	1994 Dec 09	34256	00 ^h 14 ^m 18.7 ^s	-30°23'11"
Abell 478	1991 Feb 10	22840	04 ^h 13 ^m 25.4 ^s	10°27'58"
Abell 520	1994 Mar 05	12728	04 ^h 54 ^m 10.1 ^s	02°55'27"
Abell 586	1994 Oct 06	23136	07 ^h 32 ^m 20.4 ^s	31°37'55"
PKS0745-191	1992 Oct 20	23750	07 ^h 47 ^m 31.1 ^s	-19°17'47"
Abell 665(P)	1991 Apr 10	38308	08 ^h 30 ^m 58.9 ^s	65°50'37"
IRAS09104+4109 #1	1994 Nov 08	7968	09 ^h 13 ^m 45.5 ^s	40°56'29"
IRAS09104+4109 #2	1995 Apr 12	21904	" "	" "
Abell 773	1995 Apr 15	6240	09 ^h 17 ^m 53.4 ^s	51°43'29"
Abell 963	1992 Nov 24	10104	10 ^h 17 ^m 03.4 ^s	39°02'51"
Zwicky 3146 #1	1992 Nov 27	15214	10 ^h 23 ^m 39.8 ^s	04°11'11"
Zwicky 3146 #2	1993 May 17	10831	" "	" "
Abell 1068	1995 Apr 29	15760	10 ^h 40 ^m 44.6 ^s	39°57'12"
Abell 1413(P)	1991 Nov 27	7696	11 ^h 55 ^m 18.7 ^s	23°24'12"
Abell 1689 #1	1994 Jul 22	13080	13 ^h 11 ^m 29.1 ^s	-01°20'40"
Abell 1689 #2	1995 Jun 24	9648	" "	" "
Abell 1704	1995 Apr 17	41360	13 ^h 14 ^m 24.8 ^s	64°34'39"
RXJ1347.5-1145	1995 Jan 28	15760	13 ^h 47 ^m 31 ^s	-11°45'11"
Abell 1795 #1	1992 Jun 25	2768	13 ^h 48 ^m 52.7 ^s	26°35'27"
Abell 1795 #2	1993 Jan 21	11088	" "	" "
Abell 1795 #3	1994 Jun 23	11080	" "	" "
MS1358.4+6245 #1	1991 Nov 05	2528	13 ^h 59 ^m 51.0 ^s	62°31'04"
MS1358.4+6245 #2	1993 May 14	15872	" "	" "
Abell 1835	1993 Jan 22	2850	14 ^h 01 ^m 02.0 ^s	02°52'40"
MS1455.0+2232 #1	1992 Jan 11	4088	14 ^h 57 ^m 15.0 ^s	22°20'36"
MS1455.0+2232 #2	1993 Jan 20	4230	" "	" "
MS1455.0+2232 #3	1994 Jul 07	6584	" "	" "
Abell 2029	1990 Jul 25	17758	15 ^h 10 ^m 56.2 ^s	05°44'42"
Abell 2142	1994 Jul 26	19776	15 ^h 58 ^m 20.1 ^s	27°13'52"
Abell 2163	1994 Aug 13	36248	16 ^h 15 ^m 45.9 ^s	-06°08'58"
Abell 2204	1995 Sep 01	15472	16 ^h 32 ^m 47.0 ^s	05°34'33"
Abell 2218 #1	1994 Jan 05	11520	16 ^h 35 ^m 52.5 ^s	66°12'29"
Abell 2218 #2	1994 Apr 05	27016	" "	" "
Abell 2218 #3	1994 Jun 14	30016	" "	" "
Abell 2218 #4	1994 Jun 17	24304	" "	" "
Abell 2219	1994 Jan 17	13242	16 ^h 40 ^m 20.2 ^s	46°42'29"
Abell 2261	1995 Feb 11	16288	17 ^h 22 ^m 27.3 ^s	32°07'58"
Abell 2319	1991 Mar 22	5444	19 ^h 21 ^m 12.2 ^s	43°56'38"
MS2137.3-2353	1994 Apr 24	13656	21 ^h 40 ^m 15.2 ^s	-23°39'41"
Abell 2390	1993 Nov 23	27764	21 ^h 53 ^m 36.5 ^s	17°41'45"
AC114 #1	1993 May 17	10048	22 ^h 58 ^m 48.7 ^s	-34°48'19"
AC114 #2	1994 May 09	13144	" "	" "

Notes: Columns 2 and 3 list the dates of observation and exposure times (in seconds). Where more than a single observation of a cluster was made, details for each observation are listed. Columns 4 and 5 give the coordinates of the centroids of the X-ray emission from the clusters. For Abell 665 and 1413, HRI images were not available at the time of writing and PSPC data were used for the imaging analysis. This is indicated by a (P) after the cluster name.

Table 4. Results from the spectral analysis

Parameters		Model A	Model B	Model C	Model D
Abell 2744	kT	$11.04^{+0.79}_{-0.73}$	$7.75^{+0.59}_{-0.53}$	—	$8.5^{+0.9}_{-0.7}$
	Z	$0.17^{+0.09}_{-0.09}$	$0.16^{+0.06}_{-0.06}$	—	$0.17^{+0.08}_{-0.07}$
	N_{H}	0.16	$1.44^{+0.21}_{-0.21}$	—	$1.25^{+0.14}_{-0.22}$
	\dot{M}_{S}	—	—	—	—
	kT_2	—	—	—	< 1.7
	ΔN_{H}	—	—	—	> 5.0
	L_{X}	31.3	31.0	—	30.9
	L_{Bol}	70.1	67.8	—	U.C.
χ^2/DOF		862.7/737	739.2/736	—	729.0/733
Abell 478	kT	$6.02^{+0.11}_{-0.11}$	$6.09^{+0.16}_{-0.15}$	$8.1^{+1.2}_{-0.8}$	$7.13^{+0.35}_{-0.29}$
	Z	$0.32^{+0.02}_{-0.03}$	$0.32^{+0.02}_{-0.03}$	$0.35^{+0.03}_{-0.04}$	$0.34^{+0.03}_{-0.04}$
	N_{H}	3.00	$2.94^{+0.08}_{-0.09}$	3.00	3.00
	\dot{M}_{S}	—	—	1347^{+267}_{-317}	—
	kT_2	—	—	—	$0.76^{+0.19}_{-0.12}$
	ΔN_{H}	—	—	$1.7^{+0.2}_{-0.3}$	$9.4^{+1.6}_{-1.4}$
	L_{X}	24.2	24.2	24.2	24.2
	L_{Bol}	53.8	53.5	63.6	71.6
χ^2/DOF		914.3/815	912.8/814	879.5/813	842.0/812
Abell 520	kT	$8.33^{+0.76}_{-0.67}$	$7.94^{+0.96}_{-0.90}$	—	—
	Z	$0.14^{+0.10}_{-0.10}$	$0.15^{+0.10}_{-0.10}$	—	—
	N_{H}	0.78	$0.92^{+0.23}_{-0.21}$	—	—
	\dot{M}_{S}	—	—	—	—
	kT_2	—	—	—	—
	ΔN_{H}	—	—	—	—
	L_{X}	15.8	15.7	—	—
	L_{Bol}	34.1	33.9	—	—
χ^2/DOF		431.3/430	430.2/429	—	—
Abell 586	kT	$7.15^{+0.72}_{-0.62}$	$7.02^{+0.94}_{-0.80}$	$10.7^{+10.3}_{-3.9}$	> 7.1
	Z	$0.31^{+0.13}_{-0.13}$	$0.31^{+0.13}_{-0.12}$	$0.36^{+0.16}_{-0.15}$	$0.37^{+0.17}_{-0.16}$
	N_{H}	0.52	$0.59^{+0.35}_{-0.32}$	0.52	0.52
	\dot{M}_{S}	—	—	U.C.	—
	kT_2	—	—	—	$0.9^{+4.3}_{-0.2}$
	ΔN_{H}	—	—	U.C.	$12.3^{+67.8}_{-11.1}$
	L_{X}	10.7	10.7	10.7	10.7
	L_{Bol}	22.7	22.7	26.1	31.8
χ^2/DOF		207.6/232	207.4/231	205.2/230	202.4/229
PKS0745-191	kT	$6.71^{+0.14}_{-0.14}$	$6.47^{+0.17}_{-0.19}$	$8.7^{+1.6}_{-1.2}$	$7.8^{+0.7}_{-0.5}$
	Z	$0.31^{+0.03}_{-0.03}$	$0.31^{+0.03}_{-0.02}$	$0.35^{+0.04}_{-0.03}$	$0.36^{+0.04}_{-0.04}$
	N_{H}	3.50	$3.69^{+0.10}_{-0.10}$	$3.37^{+0.46}_{-0.51}$	$3.61^{+0.22}_{-0.18}$
	\dot{M}_{S}	—	—	1455^{+356}_{-510}	—
	kT_2	—	—	—	$1.2^{+0.5}_{-0.3}$
	ΔN_{H}	—	—	$2.8^{+1.1}_{-1.3}$	$8.0^{+15.0}_{-3.5}$
	L_{X}	29.5	29.4	29.5	29.6
	L_{Bol}	65.2	65.3	74.0	77.6
χ^2/DOF		1326/1235	1315/1234	1296/1232	1270/1231

Table 4. Spectral Results - continued

	Parameters	Model A	Model B	Model C	Model D
Abell 665	kT	$9.03^{+0.58}_{-0.52}$	$8.12^{+0.62}_{-0.54}$	—	$14.2^{+10.4}_{-5.2}$
	Z	$0.22^{+0.07}_{-0.08}$	$0.23^{+0.06}_{-0.07}$	—	$0.33^{+0.11}_{-0.13}$
	N_{H}	0.42	$0.72^{+0.14}_{-0.14}$	—	$0.0^{+0.6}_{-0.0}$
	\dot{M}_{S}	—	—	—	—
	kT_2	—	—	—	< 4.4
	ΔN_{H}	—	—	—	> 2.5
	L_{X}	17.8	17.6	—	17.7
	L_{Bol}	38.5	37.9	—	U.C.
χ^2/DOF		753.1/745	740.4/744	—	732.4/741
IRAS 09104+4109	kT	$6.28^{+0.55}_{-0.48}$	$5.89^{+0.69}_{-0.62}$	$8.5^{+5.6}_{-1.8}$	$9.3^{+5.9}_{-2.7}$
	Z	$0.43^{+0.13}_{-0.12}$	$0.44^{+0.12}_{-0.12}$	$0.51^{+0.17}_{-0.15}$	$0.67^{+0.32}_{-0.30}$
	N_{H}	0.10	$0.31^{+0.26}_{-0.24}$	0.10	0.10
	\dot{M}_{S}	—	—	1655^{+645}_{-718}	—
	kT_2	—	—	—	$1.3^{+1.2}_{-1.1}$
	ΔN_{H}	—	—	$3.0^{+1.6}_{-1.3}$	$8.9^{+63.1}_{-5.6}$
	L_{X}	22.0	21.9	21.8	21.9
	L_{Bol}	46.3	46.5	55.1	65.3
χ^2/DOF		401.5/361	399.5/360	392.7/359	382.6/358
Abell 773	kT	$9.29^{+0.69}_{-0.60}$	$8.29^{+0.73}_{-0.64}$	—	—
	Z	$0.21^{+0.09}_{-0.09}$	$0.21^{+0.08}_{-0.08}$	—	—
	N_{H}	0.14	$0.42^{+0.14}_{-0.14}$	—	—
	\dot{M}_{S}	—	—	—	—
	kT_2	—	—	—	—
	ΔN_{H}	—	—	—	—
	L_{X}	14.8	14.5	—	—
	L_{Bol}	32.0	31.1	—	—
χ^2/DOF		736.0/648	724.8/647	—	—
Abell 963	kT	$6.16^{+0.34}_{-0.31}$	$6.13^{+0.45}_{-0.30}$	$6.13^{+0.67}_{-0.60}$	$6.15^{+0.35}_{-0.30}$
	Z	$0.30^{+0.08}_{-0.07}$	$0.30^{+0.08}_{-0.07}$	$0.31^{+0.07}_{-0.13}$	$0.30^{+0.11}_{-0.08}$
	N_{H}	0.14	$0.16^{+0.14}_{-0.15}$	0.14	0.14
	\dot{M}_{S}	—	—	U.C.	—
	kT_2	—	—	—	U.C.
	ΔN_{H}	—	—	U.C.	U.C.
	L_{X}	12.7	12.7	12.7	12.7
	L_{Bol}	27.0	27.0	27.0	27.0
χ^2/DOF		566.6/544	566.5/543	566.6/542	566.6/541
Zwicky 3146	kT	$6.41^{+0.26}_{-0.25}$	$6.80^{+0.38}_{-0.36}$	$11.3^{+5.8}_{-2.7}$	$10.6^{+5.0}_{-2.4}$
	Z	$0.27^{+0.06}_{-0.06}$	$0.27^{+0.06}_{-0.05}$	$0.33^{+0.07}_{-0.06}$	$0.37^{+0.08}_{-0.09}$
	N_{H}	0.30	$0.11^{+0.11}_{-0.10}$	0.30	0.30
	\dot{M}_{S}	—	—	2228^{+357}_{-636}	—
	kT_2	—	—	—	$2.6^{+1.0}_{-0.9}$
	ΔN_{H}	—	—	$1.2^{+0.3}_{-0.3}$	$0.4^{+1.6}_{-0.4}$
	L_{X}	36.9	37.2	37.3	37.4
	L_{Bol}	78.6	78.8	91.8	88.7
χ^2/DOF		724.1/735	716.3/734	699.9/733	696.0/732

Table 4. Spectral Results - continued

Parameters	Model A	Model B	Model C	Model D	
Abell 1068	kT	$4.21_{-0.14}^{+0.18}$	$3.46_{-0.13}^{+0.16}$	$5.5_{-0.9}^{+1.4}$	$16.6_{-8.6}^{+\infty}$
	Z	$0.43_{-0.08}^{+0.08}$	$0.49_{-0.08}^{+0.08}$	$0.42_{-0.08}^{+0.10}$	$0.53_{-0.11}^{+0.10}$
	N_{H}	0.14	$0.99_{-0.14}^{+0.15}$	0.14	0.14
	\dot{M}_{S}	—	—	1345_{-177}^{+145}	—
	kT_2	—	—	—	$2.5_{-0.6}^{+0.3}$
	ΔN_{H}	—	—	$3.2_{-0.8}^{+1.0}$	$1.7_{-0.4}^{+1.1}$
	L_{X}	7.00	6.66	6.80	6.95
	L_{Bol}	16.1	17.1	21.8	20.4
	χ^2/DOF	728.4/552	613.6/551	607.6/550	585.1/549
Abell 1413	kT	$7.54_{-0.27}^{+0.29}$	$6.64_{-0.28}^{+0.30}$	$8.5_{-0.8}^{+1.3}$	$9.8_{-1.1}^{+4.7}$
	Z	$0.28_{-0.05}^{+0.05}$	$0.28_{-0.05}^{+0.05}$	$0.30_{-0.05}^{+0.06}$	$0.36_{-0.07}^{+0.07}$
	N_{H}	0.22	$0.66_{-0.11}^{+0.10}$	0.22	0.22
	\dot{M}_{S}	—	—	644_{-159}^{+156}	—
	kT_2	—	—	—	$2.4_{-0.8}^{+1.5}$
	ΔN_{H}	—	—	$3.4_{-0.8}^{+1.3}$	$3.9_{-2.5}^{+3.6}$
	L_{X}	15.5	15.3	15.4	15.4
	L_{Bol}	32.9	32.8	36.4	36.6
	χ^2/DOF	992.4/954	938.9/953	934.3/952	924.7/951
Abell 1689	kT	$9.66_{-0.34}^{+0.37}$	$9.19_{-0.39}^{+0.44}$	$10.0_{-0.8}^{+1.2}$	$10.4_{-0.6}^{+0.8}$
	Z	$0.29_{-0.05}^{+0.05}$	$0.29_{-0.05}^{+0.05}$	$0.30_{-0.05}^{+0.06}$	$0.34_{-0.06}^{+0.06}$
	N_{H}	0.18	$0.32_{-0.08}^{+0.09}$	0.18	0.18
	\dot{M}_{S}	—	—	351_{-209}^{+291}	—
	kT_2	—	—	—	$1.0_{-0.4}^{+0.4}$
	ΔN_{H}	—	—	$4.1_{-1.8}^{+5.6}$	$16.2_{-5.5}^{+12.6}$
	L_{X}	32.4	32.3	32.2	32.2
	L_{Bol}	70.3	69.6	62.6	84.5
	χ^2/DOF	1085/1125	1077/1124	1075/1123	1065/1122
Abell 1704	kT	$4.73_{-0.33}^{+0.38}$	$4.20_{-0.40}^{+0.45}$	$5.7_{-1.3}^{+3.5}$	$6.1_{-1.2}^{+6.8}$
	Z	$0.34_{-0.13}^{+0.15}$	$0.39_{-0.13}^{+0.16}$	$0.38_{-0.16}^{+0.17}$	$0.39_{-0.17}^{+0.14}$
	N_{H}	0.18	$0.64_{-0.29}^{+0.31}$	0.18	0.18
	\dot{M}_{S}	—	—	987_{-616}^{+382}	—
	kT_2	—	—	—	$1.0_{-0.5}^{+1.8}$
	ΔN_{H}	—	—	$3.3_{-1.6}^{+5.2}$	$10.9_{-9.4}^{+12.1}$
	L_{X}	8.32	8.13	8.19	8.28
	L_{Bol}	18.6	19.0	22.9	30.5
	χ^2/DOF	249.1/281	241.9/280	240.2/279	234.5/278
RXJ1347.5-1145	kT	$12.46_{-0.82}^{+0.90}$	$10.44_{-0.77}^{+0.88}$	$26.4_{-12.3}^{+7.8}$	$19.3_{-4.8}^{+24.5}$
	Z	$0.38_{-0.10}^{+0.11}$	$0.34_{-0.08}^{+0.09}$	$0.43_{-0.11}^{+0.11}$	$0.55_{-0.17}^{+0.20}$
	N_{H}	0.49	$0.98_{-0.15}^{+0.16}$	0.49	0.49
	\dot{M}_{S}	—	—	3479_{-1151}^{+335}	—
	kT_2	—	—	—	$2.7_{-1.2}^{+2.4}$
	ΔN_{H}	—	—	$2.7_{-0.7}^{+3.0}$	$8.3_{-5.3}^{+13.2}$
	L_{X}	94.4	93.9	93.5	93.5
	L_{Bol}	217.8	210.7	225.0	261.8
	χ^2/DOF	803.0/741	772.7/740	764.8/739	763.9/738

Table 4. Spectral Results - continued

	Parameters	Model A	Model B	Model C	Model D
Abell 1795	kT	$5.40^{+0.08}_{-0.09}$	$5.33^{+0.10}_{-0.11}$	$5.87^{+0.29}_{-0.25}$	$7.1^{+4.6}_{-0.7}$
	Z	$0.36^{+0.03}_{-0.02}$	$0.36^{+0.03}_{-0.02}$	$0.36^{+0.03}_{-0.02}$	$0.38^{+0.04}_{-0.04}$
	N_{H}	0.12	$0.17^{+0.05}_{-0.05}$	0.12	0.12
	\dot{M}_{S}	—	—	300^{+104}_{-110}	—
	kT_2	—	—	—	$2.5^{+1.3}_{-0.6}$
	ΔN_{H}	—	—	$2.1^{+0.6}_{-0.4}$	$0.7^{+1.0}_{-0.5}$
	L_{X}	11.0	11.0	11.0	10.40
	L_{Bol}	23.6	23.6	25.2	25.6
	χ^2/DOF	1442/1236	1440/1235	1422/1234	1388/1233
MS1358.4+6245	kT	$7.48^{+0.83}_{-0.70}$	$5.75^{+0.74}_{-0.64}$	$7.5^{+7.1}_{-1.5}$	U.C.
	Z	$0.32^{+0.15}_{-0.15}$	$0.35^{+0.14}_{-0.13}$	$0.38^{+0.16}_{-0.15}$	$0.36^{+0.14}_{-0.14}$
	N_{H}	0.19	$1.04^{+0.32}_{-0.29}$	0.19	0.19
	\dot{M}_{S}	—	—	691^{+348}_{-287}	—
	kT_2	—	—	—	$5.8^{+0.7}_{-0.6}$
	ΔN_{H}	—	—	$6.4^{+8.7}_{-3.8}$	$1.8^{+1.9}_{-0.7}$
	L_{X}	10.8	10.5	10.5	10.6
	L_{Bol}	22.8	22.9	26.3	24.4
	χ^2/DOF	333.1/321	308.1/320	311.3/319	305.1/318
Abell 1835	kT	$8.21^{+0.31}_{-0.29}$	$7.33^{+0.35}_{-0.30}$	$9.8^{+2.3}_{-1.3}$	$11.1^{+4.4}_{-1.6}$
	Z	$0.35^{+0.06}_{-0.05}$	$0.34^{+0.05}_{-0.04}$	$0.40^{+0.06}_{-0.06}$	$0.47^{+0.08}_{-0.08}$
	N_{H}	0.23	$0.55^{+0.09}_{-0.09}$	0.23	0.23
	\dot{M}_{S}	—	—	1761^{+523}_{-593}	—
	kT_2	—	—	—	$2.9^{+1.2}_{-0.9}$
	ΔN_{H}	—	—	$3.2^{+1.6}_{-0.8}$	$3.1^{+3.1}_{-1.6}$
	L_{X}	45.4	44.8	44.9	44.9
	L_{Bol}	96.3	95.1	106.2	105.8
	χ^2/DOF	1292/1311	1255/1310	1247/1309	1239/1308
MS1455.0+2232	kT	$4.83^{+0.22}_{-0.21}$	$4.33^{+0.27}_{-0.25}$	$5.6^{+3.1}_{-0.9}$	$7.0^{+25.0}_{-2.0}$
	Z	$0.32^{+0.09}_{-0.07}$	$0.36^{+0.08}_{-0.07}$	$0.37^{+0.09}_{-0.08}$	$0.39^{+0.10}_{-0.09}$
	N_{H}	0.32	$0.73^{+0.17}_{-0.17}$	0.32	0.32
	\dot{M}_{S}	—	—	1728^{+714}_{-848}	—
	kT_2	—	—	—	$3.0^{+1.4}_{-1.6}$
	ΔN_{H}	—	—	$4.1^{+4.3}_{-1.6}$	$1.8^{+7.5}_{-1.1}$
	L_{X}	16.6	16.3	16.4	16.7
	L_{Bol}	37.0	37.8	44.7	39.8
	χ^2/DOF	489.7/495	472.7/494	471.3/493	468.8/492
Abell 2029	kT	$7.72^{+0.13}_{-0.13}$	$7.08^{+0.15}_{-0.14}$	$8.47^{+0.41}_{-0.36}$	$8.95^{+0.36}_{-0.31}$
	Z	$0.43^{+0.03}_{-0.03}$	$0.42^{+0.03}_{-0.03}$	$0.46^{+0.03}_{-0.03}$	$0.50^{+0.04}_{-0.03}$
	N_{H}	0.31	$0.58^{+0.04}_{-0.05}$	0.31	0.31
	\dot{M}_{S}	—	—	547^{+82}_{-81}	—
	kT_2	—	—	—	$1.6^{+0.3}_{-0.3}$
	ΔN_{H}	—	—	$3.1^{+0.5}_{-0.4}$	$6.6^{+2.1}_{-2.1}$
	L_{X}	19.9	19.9	19.9	19.9
	L_{Bol}	41.8	42.0	45.5	47.1
	χ^2/DOF	1401/1068	1289/1067	1256/1066	1226/1065

Table 4. Spectral Results - continued

	Parameters	Model A	Model B	Model C	Model D
Abell 2142	kT	$8.67^{+0.32}_{-0.30}$	$7.82^{+0.35}_{-0.32}$	$9.3^{+1.3}_{-0.7}$	$10.0^{+1.5}_{-0.7}$
	Z	$0.25^{+0.05}_{-0.05}$	$0.25^{+0.04}_{-0.05}$	$0.27^{+0.05}_{-0.05}$	$0.30^{+0.07}_{-0.07}$
	N_{H}	0.42	$0.77^{+0.10}_{-0.10}$	0.42	0.42
	\dot{M}_{S}	—	—	529^{+177}_{-164}	—
	kT_2	—	—	—	$0.9^{+1.6}_{-0.3}$
	ΔN_{H}	—	—	$3.6^{+1.8}_{-1.0}$	$15.0^{+7.5}_{-11.4}$
	L_{X}	30.4	30.4	30.4	30.4
	L_{Bol}	64.6	64.6	67.8	80.1
	χ^2/DOF	737.5/649	701.2/648	696.5/647	684.1/646
Abell 2163	kT	$13.83^{+0.78}_{-0.74}$	$10.85^{+0.71}_{-0.63}$	—	$11.8^{+1.0}_{-1.0}$
	Z	$0.23^{+0.07}_{-0.08}$	$0.22^{+0.06}_{-0.06}$	—	$0.23^{+0.07}_{-0.07}$
	N_{H}	1.21	$1.87^{+0.13}_{-0.12}$	—	$1.76^{+0.13}_{-0.14}$
	\dot{M}_{S}	—	—	—	—
	kT_2	—	—	—	< 1.5
	ΔN_{H}	—	—	—	> 10
	L_{X}	61.0	60.1	—	60.2
	L_{Bol}	147.0	137.3	—	U.C.
	χ^2/DOF	1138/1068	1047/1067	—	1037/1064
Abell 2204	kT	$7.40^{+0.30}_{-0.28}$	$6.23^{+0.30}_{-0.28}$	$9.2^{+2.5}_{-1.1}$	$13.7^{+21.3}_{-3.7}$
	Z	$0.41^{+0.06}_{-0.06}$	$0.40^{+0.06}_{-0.05}$	$0.46^{+0.07}_{-0.07}$	$0.53^{+0.10}_{-0.09}$
	N_{H}	0.57	$1.18^{+0.12}_{-0.12}$	0.57	0.57
	\dot{M}_{S}	—	—	2103^{+356}_{-378}	—
	kT_2	—	—	—	$3.8^{+1.1}_{-0.9}$
	ΔN_{H}	—	—	$3.3^{+0.9}_{-0.8}$	$1.9^{+1.4}_{-0.7}$
	L_{X}	35.2	34.5	34.6	34. 7
	L_{Bol}	74.2	73.4	85.5	82.9
	χ^2/DOF	1004/834	921.7/833	916.3/832	909.8/831
Abell 2218	kT	$7.05^{+0.36}_{-0.35}$	$7.18^{+0.50}_{-0.45}$	—	—
	Z	$0.18^{+0.06}_{-0.06}$	$0.18^{+0.06}_{-0.06}$	—	—
	N_{H}	0.32	$0.26^{+0.14}_{-0.14}$	—	—
	\dot{M}_{S}	—	—	—	—
	kT_2	—	—	—	—
	ΔN_{H}	—	—	—	—
	L_{X}	10.8	10.8	—	—
	L_{Bol}	23.1	23.1	—	—
	χ^2/DOF	710.0/694	709.4/693	—	—
Abell 2219	kT	$12.42^{+0.77}_{-0.69}$	$9.46^{+0.63}_{-0.57}$	—	$17.2^{+29.2}_{-4.5}$
	Z	$0.18^{+0.08}_{-0.08}$	$0.20^{+0.05}_{-0.06}$	—	$0.26^{+0.15}_{-0.11}$
	N_{H}	0.18	$0.77^{+0.10}_{-0.10}$	—	$0.41^{+0.31}_{-0.41}$
	\dot{M}_{S}	—	—	—	—
	kT_2	—	—	—	$1.6^{+1.4}_{-0.6}$
	ΔN_{H}	—	—	—	$7.4^{+4.7}_{-4.2}$
	L_{X}	38.9	38.0	—	38.3
	L_{Bol}	89.4	83.3	—	110.8
	χ^2/DOF	991.0/898	892.6/897	—	861.9/894

Table 4. Spectral Results - continued

	Parameters	Model A	Model B	Model C	Model D
Abell 2261	kT	$8.82^{+0.61}_{-0.54}$	$6.64^{+0.51}_{-0.46}$	$10.9^{+5.9}_{-2.2}$	$13.4^{+6.5}_{-2.6}$
	Z	$0.32^{+0.10}_{-0.09}$	$0.31^{+0.07}_{-0.08}$	$0.37^{+0.09}_{-0.09}$	$0.52^{+0.17}_{-0.15}$
	N_{H}	0.33	$1.17^{+0.17}_{-0.17}$	0.33	0.33
	\dot{M}_{S}	—	—	1323^{+215}_{-263}	—
	kT_2	—	—	—	$2.5^{+1.2}_{-0.7}$
	ΔN_{H}	—	—	$3.8^{+1.8}_{-1.4}$	$5.9^{+3.5}_{-2.7}$
	L_{X}	23.9	23.2	23.3	23.3
	L_{Bol}	51.3	50.0	58.3	61.2
χ^2/DOF		604.8/550	522.0/549	515.5/548	512.2/547
Abell 2319	kT	$9.30^{+0.41}_{-0.38}$	$8.57^{+0.45}_{-0.43}$	—	$11.3^{+1.7}_{-1.3}$
	Z	$0.33^{+0.06}_{-0.06}$	$0.33^{+0.06}_{-0.06}$	—	$0.37^{+0.09}_{-0.08}$
	N_{H}	0.80	$1.05^{+0.11}_{-0.11}$	—	$0.99^{+0.23}_{-0.20}$
	\dot{M}_{S}	—	—	—	—
	kT_2	—	—	—	$0.91^{+0.47}_{-0.27}$
	ΔN_{H}	—	—	—	$8.6^{+2.5}_{-3.2}$
	L_{X}	16.9	16.9	—	16.9
	L_{Bol}	36.8	36.7	—	43.4
χ^2/DOF		1156/1086	1140/1085	—	1106/1082
MS2137.3-2353	kT	$5.16^{+0.39}_{-0.34}$	$4.41^{+0.46}_{-0.39}$	$5.2^{+1.8}_{-0.7}$	U.C.
	Z	$0.44^{+0.14}_{-0.13}$	$0.48^{+0.14}_{-0.13}$	$0.50^{+0.15}_{-0.14}$	$0.55^{+0.24}_{-0.16}$
	N_{H}	0.36	$0.95^{+0.29}_{-0.28}$	0.36	0.36
	\dot{M}_{S}	—	—	1467^{+880}_{-726}	—
	kT_2	—	—	—	$2.6^{+4.1}_{-2.3}$
	ΔN_{H}	—	—	$6.2^{+6.1}_{-2.8}$	$3.3^{+47.7}_{-2.5}$
	L_{X}	17.0	16.6	16.6	16.7
	L_{Bol}	36.9	38.1	44.1	40.9
χ^2/DOF		239.5/279	226.1/278	226.3/277	223.5/276
Abell 2390	kT	$10.13^{+1.22}_{-0.99}$	$8.95^{+1.30}_{-1.04}$	$14.5^{+15.5}_{-5.2}$	$16.0^{+36.0}_{-5.4}$
	Z	$0.30^{+0.15}_{-0.16}$	$0.34^{+0.14}_{-0.14}$	$0.40^{+0.18}_{-0.16}$	$0.55^{+0.34}_{-0.24}$
	N_{H}	0.68	$1.11^{+0.32}_{-0.30}$	0.68	0.68
	\dot{M}_{S}	—	—	1533^{+581}_{-1112}	—
	kT_2	—	—	—	$2.5^{+3.2}_{-1.4}$
	ΔN_{H}	—	—	$2.9^{+7.6}_{-1.5}$	$5.5^{+14.9}_{-4.0}$
	L_{X}	41.3	41.0	41.0	41.1
	L_{Bol}	90.8	89.2	101.1	109.2
χ^2/DOF		327.5/344	321.9/343	320.4/342	318.3/341
AC114	kT	$9.76^{+1.04}_{-0.85}$	$8.10^{+1.01}_{-0.85}$	—	—
	Z	$0.20^{+0.12}_{-0.13}$	$0.20^{+0.10}_{-0.11}$	—	—
	N_{H}	0.13	$0.64^{+0.22}_{-0.21}$	—	—
	\dot{M}_{S}	—	—	—	—
	kT_2	—	—	—	—
	ΔN_{H}	—	—	—	—
	L_{X}	17.5	17.2	—	—
	L_{Bol}	38.1	37.0	—	—
χ^2/DOF		491.1/436	474.4/435	—	—

Table 4. Spectral Results

The best-fit parameter values and 90 per cent ($\Delta\chi^2 = 2.71$) confidence limits from the spectral analysis of the ASCA data. Temperatures (kT), metallicities (Z), column densities (N_{H}) and intrinsic column densities (ΔN_{H}) were linked to take the same values in all four detectors. With spectral models C and D, the mass deposition rates of the cooling flows (\dot{M}_{S}) and luminosities of the cooler spectral components were also linked to take the same values, but scaled by a normalization factor proportional to the total flux measured in the detector (Section 3.1). Only the normalization of the hotter isothermal emission component was allowed to vary independently for each detector. Temperatures are in keV, metallicities as a fraction of the solar value (Anders & Grevesse 1989), column densities and intrinsic column densities in units of 10^{21} atom cm^{-2} and mass deposition rates in $\text{M}_{\odot} \text{yr}^{-1}$. The \dot{M}_{S} values for model C are measured with the G3 detector. L_{X} values are the $2 - 10$ keV X-ray luminosities in the rest frame of the source. L_{Bol} values are the bolometric luminosities, corrected for the effects of Galactic and intrinsic absorption. All luminosities are in units of 10^{44} erg s^{-1} and are measured in the G3 detector. An entry of U.C. indicates that a parameter was unconstrained by the data. Note that the analysis of PKS0745-191 with spectral model C has the Galactic column density included as a free parameter (Section 3.2). The fit to Abell 2390 with spectral Model D has a second possible solution with $kT \sim 0.2$ keV and $kT_2 \sim 9.0$ keV which provides a comparable χ^2 , although this solution appears physically implausible.

Table 5. The goodness of fit for the different spectral models

Cluster	GOODNESS OF FIT				IMPROVEMENT		
	Model A	Model B	Model C	Model D	A→ B	B→ CF	B→ 2T
Abell 2744	9.9×10^{-4}	0.46	—	—	1.00	—	0.98
Abell 478	8.6×10^{-3}	8.8×10^{-3}	5.2×10^{-2}	0.23	0.77	1.00	1.00
Abell 520	0.47	0.48	—	—	0.69	—	0.57
Abell 586	0.87	0.87	0.88	0.90	0.34	0.74	0.90
PKS0745-191	1.4×10^{-3}	5.4×10^{-2}	0.10	0.22	1.00	1.00	1.00
Abell 665	0.43	0.53	—	—	1.00	—	0.96
IRAS 09104+4109	7.0×10^{-2}	7.4×10^{-2}	0.11	0.18	0.83	0.96	1.00
Abell 773	9.1×10^{-3}	1.8×10^{-2}	—	—	1.00	—	0.82
Abell 963	0.24	0.24	0.23	0.22	0.24	0.00	0.00
Zwicky 3146	0.61	0.67	0.81	0.83	0.99	1.00	1.00
Abell 1068	6.0×10^{-7}	3.3×10^{-2}	4.5×10^{-2}	0.14	1.00	0.93	1.00
Abell 1413	0.19	0.62	0.65	0.72	1.00	0.91	1.00
Abell 1689	0.80	0.84	0.85	0.89	1.00	0.84	0.99
Abell 1704	0.92	0.95	0.96	0.97	0.90	0.63	0.97
RXJ1347.5-1145	5.7×10^{-2}	0.20	0.25	0.26	1.00	0.98	0.96
Abell 1795	4.0×10^{-5}	4.3×10^{-5}	1.5×10^{-4}	1.3×10^{-3}	0.83	1.00	1.00
MS1358.4+6245	0.31	0.67	0.61	0.69	1.00	0.00	0.64
Abell 1835	0.64	0.86	0.89	0.91	1.00	0.99	1.00
MS1455.0+2232	0.56	0.75	0.75	0.77	1.00	0.52	0.80
Abell 2029	< 10^{-7}	3.0×10^{-6}	4.7×10^{-5}	4.2×10^{-4}	1.00	1.00	1.00
Abell 2142	8.9×10^{-3}	7.3×10^{-2}	8.7×10^{-2}	0.15	1.00	0.92	1.00
Abell 2163	6.7×10^{-2}	0.66	—	—	1.00	—	0.98
Abell 2204	4.3×10^{-5}	1.7×10^{-2}	2.2×10^{-2}	2.9×10^{-2}	1.00	0.97	0.99
Abell 2218	0.33	0.33	—	—	0.55	—	0.50
Abell 2219	1.6×10^{-2}	0.54	—	—	1.00	—	1.00
Abell 2261	5.3×10^{-2}	0.79	0.84	0.85	1.00	0.97	0.99
Abell 2319	6.9×10^{-2}	0.12	—	—	1.00	—	1.00
MS2137.3-2353	0.96	0.99	0.99	0.99	1.00	0.00	0.65
Abell 2390	0.73	0.79	0.79	0.81	0.97	0.55	0.88
AC114	3.5×10^{-2}	9.3×10^{-2}	—	—	1.00	—	0.20

The goodness of fit results for spectral models A–D, listing the probabilities of exceeding the best-fitting reduced χ^2 values, assuming in each case that the model correctly describes the data. Column 6 lists the significance of the improvements to the fits obtained with model B over model A (*i.e.* including the Galactic column density as a free parameter in the isothermal model). Columns 7 and 8 list the significance of the improvements obtained by using the multiphase spectral models [either the cooling flow (CF) or two-temperature models (2T)] in preference to the single-phase model B.

Table 6. Results from the deprojection analysis of the ROSAT images

Cluster	binsize (arcsec/kpc)	MASS PROFILES			DEPROJECTION RESULTS		
		σ (km s^{-1})	r_c (kpc)	t_{cool} (10^9 yr)	\bar{t}_{100} (10^9 yr)	r_{cool} (kpc)	\dot{M}_I ($\text{M}_\odot \text{yr}^{-1}$)
Abell 2744	16/89.4	1120^{+40}_{-50}	450	$18.8^{+42.0}_{-6.4}$	19.2	< 134	< 101
Abell 478	12/26.5	860^{+70}_{-50}	70	$1.1^{+0.1}_{-0.1}$	3.11	222^{+30}_{-50}	810^{+176}_{-195}
Abell 520	24/102	980^{+10}_{-60}	450	$16.7^{+24.0}_{-6.2}$	16.3	< 154	< 85
Abell 586	16/60.3	1050^{+450}_{-250}	130	$5.5^{+0.7}_{-0.7}$	7.94	119^{+31}_{-29}	159^{+69}_{-56}
PKS0745-191	12/30.3	930^{+90}_{-70}	37.5	$1.1^{+0.1}_{-0.1}$	2.65	178^{+19}_{-12}	650^{+120}_{-148}
Abell 665	30/118	930^{+30}_{-30}	200	$12.3^{+0.9}_{-0.9}$	13.0	< 177	< 232
IRAS 09104+4109	12/81.0	1120^{+330}_{-120}	45	$2.0^{+0.1}_{-0.1}$	2.32	193^{+90}_{-72}	620^{+147}_{-87}
Abell 773	16/71.5	990^{+70}_{-50}	180	$9.8^{+13.7}_{-6.6}$	11.2	< 179	< 238
Abell 963	16/69.0	750^{+50}_{-50}	80	$4.1^{+1.3}_{-0.5}$	5.60	188^{+53}_{-84}	340^{+129}_{-183}
Zwicky 3146	12/64.8	1150^{+280}_{-140}	50	$1.7^{+0.1}_{-0.1}$	2.53	205^{+21}_{-43}	1057^{+117}_{-146}
Abell 1068	12/38.6	780^{+90}_{-70}	30	$1.2^{+0.1}_{-0.1}$	2.75	185^{+65}_{-50}	408^{+128}_{-90}
Abell 1413	30/98.7	960^{+70}_{-50}	130	$8.6^{+0.6}_{-0.7}$	8.63	119^{+29}_{-70}	137^{+43}_{-85}
Abell 1689	12/47.7	990^{+60}_{-50}	80	$2.9^{+0.5}_{-0.2}$	4.34	180^{+35}_{-61}	563^{+185}_{-174}
Abell 1704	12/53.5	750^{+220}_{-90}	30	$2.1^{+0.1}_{-0.2}$	3.59	187^{+53}_{-54}	306^{+92}_{-73}
RXJ1347.5-1145	12/81.7	1850^{+270}_{-500}	75	$2.6^{+0.2}_{-0.1}$	3.00	196^{+90}_{-73}	1378^{+75}_{-316}
Abell 1795	16/26.3	740^{+20}_{-20}	50	$1.4^{+0.1}_{-0.1}$	3.42	188^{+11}_{-16}	449^{+46}_{-46}
MS1358.4+6245	8/46.3	830^{+340}_{-80}	40	$2.8^{+1.2}_{-0.6}$	4.76	113^{+187}_{-44}	123^{+369}_{-50}
Abell 1835	8/39.5	1000^{+120}_{-70}	50	$1.5^{+0.5}_{-0.3}$	2.44	231^{+26}_{-14}	1154^{+432}_{-482}
MS1455.0+2232	8/40.1	760^{+190}_{-70}	45	$1.1^{+0.2}_{-0.1}$	2.15	215^{+45}_{-35}	712^{+185}_{-53}
Abell 2029	16/31.5	880^{+40}_{-30}	80	$1.5^{+0.1}_{-0.1}$	3.54	193^{+42}_{-20}	576^{+99}_{-79}
Abell 2142	16/35.7	910^{+70}_{-40}	100	$4.3^{+0.8}_{-0.7}$	5.38	154^{+42}_{-29}	303^{+167}_{-72}
Abell 2163	12/52.1	1210^{+30}_{-40}	300	$12.7^{+12.3}_{-4.6}$	12.1	< 130	< 90
Abell 2204	12/41.4	1020^{+130}_{-60}	25	$0.94^{+0.04}_{-0.04}$	2.01	235^{+34}_{-90}	1007^{+98}_{-263}
Abell 2218	16/61.4	830^{+30}_{-40}	230	$10.4^{+4.1}_{-2.0}$	12.8	< 153	< 133
Abell 2219	10/46.2	1050^{+50}_{-50}	250	$9.0^{+18.8}_{-3.8}$	10.7	< 254	< 485
Abell 2261	8/36.6	1030^{+240}_{-120}	80	$3.0^{+1.4}_{-0.6}$	5.63	125^{+76}_{-34}	227^{+238}_{-87}
Abell 2319	32/47.4	890^{+30}_{-20}	150	$9.5^{+10.4}_{-3.2}$	9.81	109^{+55}_{-39}	80^{+81}_{-47}
MS2137.3-2353	12/67.7	830^{+140}_{-50}	32	$1.2^{+0.1}_{-0.1}$	1.65	216^{+156}_{-47}	754^{+263}_{-117}
Abell 2390	16/75.1	1190^{+520}_{-240}	60	$4.2^{+0.3}_{-0.2}$	5.45	146^{+41}_{-34}	370^{+97}_{-69}
AC114	12/67.6	1030^{+60}_{-40}	300	$16.9^{+32.7}_{-6.2}$	16.6	< 135	< 120

Notes: Column 2 lists the binsize (in arcsec and kpc) used in the analysis. Columns 3 and 4 summarize the velocity dispersions and core radii used to parameterize the mass profiles (Section 4). Columns 5 and 6 list the cooling times *i.e.* the time for the gas to cool from the ambient cluster temperature at constant pressure (in units of 10^9 yr) within the central bin and within a fixed radius of 100 kpc (t_{cool} and \bar{t}_{100} , respectively). Cooling radii (r_{cool}) are the radii where the cooling time of the cluster gas becomes equal to the age of the Universe (1.3×10^{10} yr). Mass deposition rates (\dot{M}_I) are the integrated mass deposition rates within the cooling radii in $\text{M}_\odot \text{yr}^{-1}$. Errors on the velocity dispersions are 90 per cent confidence limits. Errors on the cooling times are the 10 and 90 percentile values from 100 Monte Carlo simulations, using the best-fit mass models for the clusters. The upper and lower confidence limits on the cooling radii are the points where the 10 and 90 percentiles exceed and become less than the Hubble time, respectively. Errors on the mass deposition rates are the 90 and 10 percentile values at the upper and lower limits for the cooling radius. For Abell 478, 586, 1795, 2029 and 2219, the introduction of a second mass component was found to improve the isothermality of the temperature profile and for these clusters the multi-component mass models (described in Section 4) have been used in determining the deprojection results. We note that the errors on the deprojection results do not account for the uncertainties in the total mass profiles.

Table 7. Absorption-corrected mass deposition rates

Cluster	INTRINSIC ABSORPTION	ORIGINAL DEPROJ.	CORRECTED DEPROJ.	SPECTRAL ANALYSIS
	ΔN_{H} (10^{21} atom cm $^{-2}$)	\dot{M}_{I} (M_{\odot} yr $^{-1}$)	\dot{M}_{C} (M_{\odot} yr $^{-1}$)	\dot{M}_{S} (M_{\odot} yr $^{-1}$)
Abell 478	$1.7^{+0.2}_{-0.3}$	810^{+176}_{-195}	1059^{+421}_{-300}	1347^{+267}_{-317}
PKS0745-191	$2.8^{+1.1}_{-1.1}$	650^{+120}_{-148}	950^{+166}_{-200}	1455^{+356}_{-510}
IRAS 09104+4109	$3.0^{+1.6}_{-0.3}$	620^{+147}_{-87}	1060^{+356}_{-222}	1655^{+645}_{-718}
Zwicky 3146	$1.2^{+0.3}_{-0.3}$	1057^{+117}_{-146}	1358^{+149}_{-205}	2228^{+357}_{-636}
Abell 1068	$3.2^{+1.0}_{-0.8}$	408^{+128}_{-90}	937^{+185}_{-186}	1345^{+145}_{-177}
Abell 1413	$3.4^{+1.3}_{-0.8}$	137^{+43}_{-85}	321^{+173}_{-55}	644^{+156}_{-159}
Abell 1689	$4.1^{+5.6}_{-1.8}$	563^{+185}_{-174}	2016^{+1575}_{-908}	351^{+291}_{-209}
Abell 1704	$3.3^{+5.2}_{-1.6}$	306^{+92}_{-73}	632^{+793}_{-158}	987^{+382}_{-616}
RXJ1347.5-1145	$2.7^{+3.0}_{-0.7}$	1378^{+75}_{-316}	1790^{+413}_{-411}	3479^{+335}_{-1151}
Abell 1795	$2.1^{+0.6}_{-0.4}$	449^{+46}_{-46}	1038^{+229}_{-144}	300^{+104}_{-110}
MS1358.4+6245	$6.4^{+8.7}_{-3.8}$	123^{+369}_{-50}	703^{+1668}_{-445}	691^{+348}_{-287}
Abell 1835	$3.2^{+1.6}_{-0.8}$	1154^{+432}_{-482}	2111^{+2154}_{-921}	1761^{+523}_{-593}
MS1455.0+2232	$4.1^{+4.3}_{-1.6}$	712^{+185}_{-53}	1227^{+715}_{-172}	1728^{+714}_{-848}
Abell 2029	$3.1^{+0.5}_{-0.4}$	576^{+99}_{-79}	1220^{+223}_{-160}	547^{+82}_{-81}
Abell 2142	$3.6^{+1.8}_{-1.0}$	303^{+167}_{-72}	1303^{+409}_{-653}	529^{+177}_{-164}
Abell 2204	$3.3^{+0.9}_{-0.8}$	1007^{+98}_{-263}	1660^{+634}_{-232}	2103^{+356}_{-378}
Abell 2261	$3.8^{+1.8}_{-1.4}$	227^{+238}_{-87}	680^{+248}_{-164}	1323^{+315}_{-293}
MS2137.3-2353	$6.2^{+6.1}_{-2.8}$	754^{+263}_{-117}	1537^{+1499}_{-399}	1467^{+880}_{-726}
Abell 2390	$2.9^{+7.6}_{-1.5}$	370^{+97}_{-69}	599^{+852}_{-163}	1533^{+581}_{-1112}

A comparison of the mass deposition rates measured from the deprojection analysis, corrected for the effects of intrinsic absorption due to cold gas (\dot{M}_{C}), with the values determined from the spectral analysis (\dot{M}_{S}). Errors on the corrected deprojection values account for the statistical uncertainties in both the deprojected quantities and intrinsic column densities. No entries are listed for Abell 586 or 963 since the spectral data do not constrain the mass deposition rates and intrinsic column densities for these systems.

Table 8. Cooling flow flux fractions

Cluster	$(L_{\text{cool}}/L_{\text{X}})$
Abell 478	$0.37^{+0.15}_{-0.12}$
PKS0745-191	$0.36^{+0.19}_{-0.17}$
IRAS 09104+4109	$0.55^{+0.45}_{-0.32}$
Zwicky 3146	$0.63^{+0.37}_{-0.31}$
Abell 1068	$0.74^{+0.26}_{-0.20}$
Abell 1413	$0.30^{+0.13}_{-0.09}$
Abell 1689	$0.10^{+0.10}_{-0.06}$
Abell 1704	$0.48^{+0.52}_{-0.36}$
RXJ1347.5-1145	$0.90^{+0.10}_{-0.57}$
Abell 1795	$0.11^{+0.05}_{-0.05}$
MS1358.4+6245	$0.38^{+0.62}_{-0.18}$
Abell 1835	$0.34^{+0.22}_{-0.15}$
MS1455.0+2232	$0.40^{+0.60}_{-0.24}$
Abell 2029	$0.21^{+0.04}_{-0.04}$
Abell 2142	$0.13^{+0.07}_{-0.05}$
Abell 2204	$0.49^{+0.25}_{-0.14}$
Abell 2261	$0.59^{+0.18}_{-0.20}$
MS2137.3-2353	$0.29^{+0.40}_{-0.16}$
Abell 2390	$0.51^{+0.49}_{-0.42}$

Notes: The fractions of the 2–10 keV X-ray luminosities contributed by the cooling flows (determined with spectral model C and measured in the G3 detector). The errors are 90 per cent confidence limits.

Table 9. The column densities of intrinsic X-ray absorbing material

Cluster	CF CLUSTERS					<i>f</i>	Cluster	NCFs	
	B-A	C-A	C'-A	D-A				B-A	
Abell 478	$-0.06^{+0.08}_{-0.09}$	$1.7^{+0.2}_{-0.3}$	$0.83^{+0.28}_{-0.38}$	$9.4^{+1.6}_{-1.4}$	> 0.85		Abell 2744	$1.28^{+0.21}_{-0.21}$	
Abell 586	$0.07^{+0.35}_{-0.32}$	—	$0.85^{+0.34}_{-0.93}$	$12.3^{+67.8}_{-11.1}$	U.C.		Abell 520	$0.14^{+0.23}_{-0.21}$	
PKS0745-191*	$0.19^{+0.10}_{-0.10}$	$2.8^{+1.1}_{-1.3}$	$1.09^{+0.29}_{-0.57}$	$8.0^{+15.0}_{-3.5}$	> 0.89		Abell 665	$0.30^{+0.14}_{-0.14}$	
IRAS 09104+4109	$0.21^{+0.26}_{-0.24}$	$3.0^{+1.6}_{-1.3}$	$0.93^{+0.36}_{-0.80}$	$8.9^{+63.1}_{-5.6}$	> 0.79		Abell 773	$0.28^{+0.14}_{-0.14}$	
Abell 963	$0.02^{+0.14}_{-0.15}$	—	$0.01^{+0.21}_{-0.11}$	—	U.C.		Abell 2163	$0.66^{+0.13}_{-0.12}$	
Zwicky 3146	$-0.19^{+0.11}_{-0.10}$	$1.2^{+0.3}_{-0.3}$	$0.53^{+0.17}_{-0.26}$	$0.4^{+1.6}_{-0.4}$	> 0.42		Abell 2218	$-0.06^{+0.14}_{-0.14}$	
Abell 1068	$0.85^{+0.15}_{-0.14}$	$3.2^{+1.0}_{-0.8}$	$1.19^{+0.44}_{-0.39}$	$1.7^{+1.1}_{-0.4}$	> 0.95		Abell 2219	$0.59^{+0.10}_{-0.10}$	
Abell 1413	$0.44^{+0.10}_{-0.11}$	$3.4^{+1.3}_{-0.8}$	$0.53^{+0.36}_{-0.19}$	$3.9^{+3.6}_{-2.5}$	> 0.89		Abell 2319	$0.25^{+0.11}_{-0.11}$	
Abell 1689	$0.14^{+0.09}_{-0.08}$	$4.1^{+5.6}_{-1.8}$	$0.19^{+0.12}_{-0.24}$	$16.2^{+12.6}_{-5.5}$	> 0.59		AC114	$0.51^{+0.22}_{-0.21}$	
Abell 1704	$0.46^{+0.31}_{-0.29}$	$3.3^{+5.2}_{-1.6}$	$0.45^{+1.38}_{-0.24}$	$10.9^{+12.1}_{-9.4}$	> 0.79				
RXJ1347.5-1145	$0.49^{+0.16}_{-0.15}$	$2.7^{+3.0}_{-0.7}$	$1.05^{+0.17}_{-0.17}$	$8.3^{+13.2}_{-5.3}$	> 0.58				
Abell 1795	$0.05^{+0.05}_{-0.05}$	$2.1^{+0.6}_{-0.4}$	$0.17^{+0.11}_{-0.11}$	$0.7^{+1.0}_{-0.5}$	> 0.76				
MS1358.4+6245	$0.85^{+0.32}_{-0.29}$	$6.4^{+8.7}_{-3.8}$	$0.97^{+0.55}_{-0.22}$	$1.8^{+1.3}_{-0.7}$	> 0.80				
Abell 1835	$0.32^{+0.09}_{-0.09}$	$3.2^{+1.6}_{-0.8}$	$0.63^{+0.34}_{-0.35}$	$3.1^{+3.1}_{-1.6}$	> 0.80				
MS1455.0+2232	$0.41^{+0.17}_{-0.17}$	$4.1^{+4.3}_{-1.6}$	$0.65^{+0.84}_{-0.36}$	$1.8^{+7.5}_{-1.5}$	> 0.63				
Abell 2029	$0.27^{+0.04}_{-0.05}$	$3.1^{+0.5}_{-0.4}$	$0.45^{+0.10}_{-0.09}$	$6.6^{+2.1}_{-2.1}$	> 0.91				
Abell 2142	$0.35^{+0.10}_{-0.10}$	$3.6^{+1.8}_{-1.0}$	$0.35^{+0.27}_{-0.08}$	$15.0^{+7.5}_{-11.4}$	> 0.80				
Abell 2204	$0.61^{+0.12}_{-0.12}$	$3.3^{+0.9}_{-0.8}$	$1.02^{+0.37}_{-0.38}$	$1.9^{+1.4}_{-0.7}$	> 0.93				
Abell 2261	$0.84^{+0.17}_{-0.17}$	$3.8^{+1.8}_{-1.4}$	$1.51^{+0.39}_{-0.61}$	$5.9^{+3.5}_{-2.7}$	> 0.84				
MS2137.3-2353	$0.59^{+0.29}_{-0.28}$	$6.2^{+6.1}_{-2.8}$	$0.60^{+0.39}_{-0.19}$	$3.3^{+47.7}_{-2.5}$	> 0.87				
Abell 2390	$0.43^{+0.32}_{-0.30}$	$2.9^{+7.6}_{-1.5}$	$1.17^{+0.42}_{-0.88}$	$5.5^{+14.9}_{-4.0}$	> 0.57				
MEAN	0.35 ± 0.30	3.4 ± 1.3	0.72 ± 0.39	6.3 ± 4.7			MEAN	0.44 ± 0.39	

A summary of the results on intrinsic absorption from the ASCA data. Columns 2 – 5 list the differences between the spectrally-determined column densities and the nominal Galactic values for spectral models B, C, D and C'. Also listed are the (90 per cent confidence) constraints on the covering fraction of the intrinsic absorber, *f*, using spectral model C. All results assume solar metallicity in the absorbing material. For PKS0745-191*, the ASCA data indicate a Galactic column density 3.5×10^{21} atom cm $^{-2}$ which is lower than the nominal value of 4.24×10^{21} atom cm $^{-2}$ (Dickey & Lockman 1990). The lower value of 3.5×10^{21} atom cm $^{-2}$ has been used in the calculation of the intrinsic column densities. The errors on the mean values are the standard deviations of the distributions.

Table 10. The masses of intrinsic X-ray absorbing gas

Cluster	r_{abs} (kpc)	M_{abs} [Z_{\odot}] ($10^{11} M_{\odot}$)	M_{abs} [Z_{ICM}] ($10^{11} M_{\odot}$)	$\dot{M}(r < r_{\text{abs}})$ ($10^9 M_{\odot} \text{ yr}^{-1}$)	M_{acc} ($10^{11} M_{\odot}$)
Abell 478	115^{+31}_{-22}	$7.30^{+4.60}_{-2.61}$	$14.60^{+9.21}_{-5.22}$	628^{+204}_{-150}	$15.70^{+5.10}_{-3.75}$
PKS0745-191	121^{+45}_{-45}	$13.31^{+12.72}_{-8.30}$	$26.61^{+25.44}_{-16.60}$	909^{+144}_{-344}	$22.73^{+3.60}_{-8.60}$
IRAS 09104+4109	120^{+82}_{-80}	$14.02^{+27.83}_{-12.53}$	$28.05^{+55.66}_{-25.06}$	911^{+292}_{-361}	$22.77^{+7.30}_{-9.03}$
Zwicky 3146	119^{+42}_{-22}	$5.52^{+4.83}_{-1.94}$	$11.03^{+9.67}_{-3.89}$	1050^{+269}_{-145}	$26.25^{+6.73}_{-3.63}$
Abell 1068	135^{+38}_{-39}	$18.93^{+13.13}_{-9.60}$	$37.86^{+26.26}_{-19.19}$	769^{+232}_{-223}	$19.23^{+5.80}_{-5.58}$
Abell 1689	123^{+44}_{-43}	$20.13^{+22.05}_{-11.99}$	$40.27^{+44.10}_{-23.98}$	862^{+890}_{-347}	$21.55^{+22.25}_{-8.68}$
Abell 1704	99^{+69}_{-19}	$10.50^{+24.50}_{-3.98}$	$21.00^{+49.00}_{-7.95}$	386^{+536}_{-106}	$9.65^{+13.40}_{-2.65}$
RXJ1347.5-1145	114^{+90}_{-73}	$11.39^{+29.14}_{-9.95}$	$22.78^{+58.27}_{-19.91}$	1440^{+708}_{-748}	$36.00^{+17.70}_{-18.70}$
Abell 1795	124^{+22}_{-29}	$10.48^{+4.46}_{-4.45}$	$20.96^{+8.93}_{-8.89}$	645^{+137}_{-163}	$16.13^{+3.43}_{-4.08}$
MS1358.4+6245	79^{+65}_{-50}	$12.97^{+35.97}_{-11.32}$	$25.93^{+71.94}_{-22.64}$	232^{+811}_{-133}	$5.80^{+20.27}_{-3.33}$
Abell 1835	129^{+49}_{-67}	$17.29^{+17.37}_{-13.39}$	$34.57^{+34.54}_{-26.78}$	1430^{+1307}_{-632}	$35.75^{+32.67}_{-15.80}$
MS1455.0+2232	181^{+39}_{-81}	$43.60^{+27.87}_{-30.81}$	$87.20^{+55.14}_{-61.62}$	1596^{+613}_{-613}	$39.90^{+15.32}_{-18.73}$
Abell 2029	126^{+15}_{-17}	$15.98^{+4.35}_{-4.17}$	$31.95^{+8.71}_{-8.35}$	839^{+152}_{-128}	$20.98^{+3.80}_{-3.20}$
Abell 2142	93^{+32}_{-40}	$10.11^{+9.06}_{-6.92}$	$20.21^{+18.13}_{-13.83}$	374^{+219}_{-201}	$9.35^{+5.47}_{-5.03}$
Abell 2204	136^{+50}_{-33}	$19.81^{+18.26}_{-8.72}$	$39.63^{+36.51}_{-17.45}$	1337^{+415}_{-271}	$33.43^{+10.38}_{-6.78}$
Abell 2261	94^{+34}_{-76}	$10.90^{+10.27}_{-10.51}$	$21.80^{+20.54}_{-21.03}$	329^{+201}_{-301}	$8.23^{+5.03}_{-7.53}$
MS2137.3-2353	170^{+67}_{-68}	$58.16^{+66.00}_{-38.17}$	$116.32^{+132.00}_{-76.34}$	1643^{+1162}_{-563}	$41.08^{+29.05}_{-14.08}$
Abell 2390	62^{+50}_{-25}	$3.62^{+11.28}_{-2.40}$	$7.24^{+22.57}_{-4.79}$	293^{+573}_{-99}	$7.33^{+14.33}_{-2.47}$

Notes: r_{abs} values are the radii at which the cooling time of the gas first exceeds 5×10^9 yr, determined from the absorption-corrected deprojection results. M_{abs} values are the masses of absorbing material within radii r_{abs} implied by the observed intrinsic column densities (determined with spectral model C) assuming the absorption to be due to cold gas with solar metallicity (column 3) or $Z = 0.4Z_{\odot}$ (column 4). Column 5 lists the integrated mass deposition rates (corrected for the effects of absorption) within radii r_{abs} . M_{acc} values are the masses of material accumulated within radii r_{abs} during the first 5 Gyr. Errors incorporate the statistical uncertainties in both the intrinsic column densities (determined with spectral model C) and the deprojection results. Errors on the r_{abs} values are the 10 and 90 percentile values from 100 Monte Carlo simulations. Errors on the M_{abs} values are the extrema incorporating the joint errors in r_{abs} and ΔN_{abs} . Results are not tabulated for Abell 1413 since the central cooling time in this cluster exceeds 5 Gyr.

Table 11. The reprocessed luminosities and observed IRAS fluxes

Cluster	$L_{\text{repro.}}$ (10^{44} erg s $^{-1}$)	S_{60} (mJy)	S_{100} (mJy)	ΔR (arcmin)	$L_{1-1000\mu\text{m}}$ (10^{44} erg s $^{-1}$)
Abell 478	10.5	570 ± 58	5490 ± 440	0.55	60 ± 19
PKS0745-191	13.4	< 294	< 1680	—	< 29.0
IRAS 09104+4109	13.3	560 ± 39	< 324	—	< 390
Zwicky 3146	6.15	< 111	880 ± 56	1.53	< 111
Abell 1068	9.05	680 ± 38	950 ± 108	0.02	59 ± 18
Abell 1413	5.71	< 111	< 333	—	< 14.2
Abell 1689	3.46	< 141	< 357	—	< 27.3
Abell 1704	6.84	90 ± 41	280 ± 83	0.43	27 ± 11
RXJ1347.5-1145	49.7	< 141	< 498	—	< 196
Abell 1795	1.95	< 144	< 354	—	< 3.23
MS1358.4+6245	6.45	< 81	< 222	—	< 51.6
Abell 1835	16.7	140 ± 64	< 504	0.05	< 61.5
MS1455.0+2232	12.3	< 96	< 378	—	< 46.6
Abell 2029	5.13	< 96	< 351	—	< 3.98
Abell 2142	5.47	130 ± 51	480 ± 156	2.50	7.2 ± 2.9
Abell 2204	19.2	< 288	1760 ± 306	2.58	< 64.8
Abell 2261	14.9	150 ± 30	410 ± 53	1.66	45 ± 15
MS2137.3-2353	11.0	< 69	< 249	—	< 46.9
Abell 2390	17.4	130 ± 60	750 ± 207	1.73	66 ± 26

Notes: Column 2 lists the X-ray luminosities expected to be reprocessed into far infrared emission by the intrinsic absorbing material in the clusters. The best-fit parameters determined with spectral model C have been used in the calculations. Columns 3 and 4 lists the observed 60 and 100 μm IRAS fluxes within a 4 arcmin (radius) aperture centered on the X-ray centres (Table 3), determined with the IPAC SCANPI software and co-added IRAS scans (we use the median of the coadded scans). Error bars are the root-mean-square deviations in the residuals, external to the source extraction regions, after baseline subtraction. Where no clear detection was made, an upper limit equal to three times the r.m.s. deviation in the residuals is given (although systematic errors could exceed these limits in individual cases). Where a possible detection is made, Column 6 lists the in-scan separation, ΔR (in arcmin), between the peak of the 100 μm emission (or 60 μm emission in the case of Abell 1835) and the X-ray centre. Column 7 lists the total 1 – 1000 μm luminosities calculated using equation 4.